

Phase-dependent microwave response of a graphene Josephson junction

R. Haller,^{1,*} G. Fülöp,^{1,2} D. Indolese,¹ J. Ridderbos,¹ R. Kraft,^{3,4} L. Y. Cheung,¹ J. H. Ungerer,^{1,5} K. Watanabe,⁶ T. Taniguchi,⁷ D. Beckmann,⁸ R. Danneau,⁸ P. Virtanen,⁹ and C. Schönenberger^{1,5,†}

¹*Department of Physics, University of Basel, Klingelbergstrasse 82 CH-4056, Switzerland*

²*Department of Physics, Budapest University of Technology and Economics and MTA-BME*

“Momentum” Nanoelectronics Research Group, H-1111 Budapest, Budafoki út 8., Hungary

³*Institute of Nanotechnology, Karlsruhe Institute of Technology, D-76021 Karlsruhe, Germany*

⁴*Institute of Physics, Karlsruhe Institute of Technology, D-76131 Karlsruhe, Germany*

⁵*Swiss Nanoscience Institute, University of Basel, Klingelbergstrasse 82 CH-4056, Switzerland*

⁶*Research Center for Functional Materials,*

National Institute for Materials Science, 1-1 Namiki, Tsukuba 305-0044, Japan

⁷*International Center for Materials Nanoarchitectonics,*

National Institute for Materials Science, 1-1 Namiki, Tsukuba 305-0044, Japan

⁸*Institute of Quantum Materials and Technologies,*

Karlsruhe Institute of Technology, D-76021 Karlsruhe, Germany

⁹*Department of Physics and Nanoscience Center, University of Jyväskylä,*

P.O. Box 35 (YFL), University of Jyväskylä FI-40014, Finland

(Dated: February 18, 2022)

Gate-tunable Josephson junctions embedded in a microwave environment provide a promising platform to in-situ engineer and optimize novel superconducting quantum circuits. The key quantity for the circuit design is the phase-dependent complex admittance of the junction, which can be probed by sensing an rf SQUID with a tank circuit. Here, we investigate a graphene-based Josephson junction as a prototype gate-tunable element enclosed in a SQUID loop that is inductively coupled to a superconducting resonator operating at 3 GHz. With a concise circuit model that describes the dispersive and dissipative response of the coupled system, we extract the phase-dependent junction admittance corrected for self-screening of the SQUID loop. We decompose the admittance into the current-phase relation and the phase-dependent loss and as these quantities are dictated by the spectrum and population dynamics of the supercurrent-carrying Andreev bound states, we gain insight to the underlying microscopic transport mechanisms in the junction. We theoretically reproduce the experimental results by considering a short, diffusive junction model that takes into account the interaction between the Andreev spectrum and the electromagnetic environment, from which we deduce a lifetime of ~ 17 ps for non-equilibrium populations.

I. INTRODUCTION

For Josephson junctions (JJs), in which the superconducting electrodes are linked with a short normal-conducting region, the coherent superconducting interaction is promoted by so-called Andreev bound states (ABSs) [1]. The material and geometrical properties of the weak link together with the superconducting phase difference φ across the JJ define the energy of the ABSs [2]. Their structure and occupation dynamics determine the inductive and dissipative microwave response, i.e. the admittance of the JJ [3, 4]. In particular, the inductive response relates to the time-averaged dispersion of the populated ABSs and reflects the phase dependence of the supercurrent $I_s(\varphi)$ across the junction [5, 6], which is known as the current-phase relation (CPR). On the other hand, the dissipative response relates to the fluctuations in the ABS population resulting in temporal changes of the supercurrent [7, 8]. The microscopic source for those dynamics are thermally

activated or microwave induced short-lived ABS excitations [9]. Conclusively, the junction admittance, which is the key quantity to engineer high-frequency Josephson circuits, is highly dependent on the underlying microscopic processes.

The junction admittance can be probed as a function of phase by embedding a JJ in an rf SQUID that couples to a resonator [9–13]. The rf SQUID acts as a magnetic flux-tunable complex impedance in the circuit that shifts and broadens the resonance behavior, from which one can infer the phase-dependent inductive and dissipative response of the junction [14]. The strong demand for in-situ controllable junctions in microwave applications has raised the attention to JJs consisting of gate-tunable weak links [15]. Here, we determine the full complex admittance of a Josephson weak link made of graphene, which is a two-dimensional (2D) material with a linear band structure and excellent gating properties.

Although graphene JJs have already demonstrated their compatibility in different superconducting high-frequency circuits, such as bolometers [16, 17], transmon qubits [18, 19] and tunable microwave cavities [20], only few experiments have addressed the determination of their phase-dependent admittance [13, 21]. While Ref. [13] has been focusing on the phase-dependent dis-

* roy.haller@unibas.ch

† <http://www.nanoelectronics.unibas.ch/>

sipation of the junction under the influence of external irradiation and Ref. [21] on the inductive behaviour, we here investigate both the inductive and dissipative response simultaneously by studying the inherent photonic phase-dependent interplay between the sensing resonator and the graphene JJ. We present a classical, comprehensive circuit model to infer the full complex junction admittance from the reflective response of a graphene rf SQUID coupled to a superconducting microwave resonator operating at ~ 3 GHz. We further translate this to the CPR and the phase-dependent dissipation as a function of gate voltage, under consideration of the self-screening effect that arises due to the finite inductance of the SQUID loop. We describe our observations within the framework of ABSs and find remarkable agreement between the experimental results and the theoretically predicted microwave response of a short, diffusive junction.

II. DEVICE

The device is presented in Fig.1 and consists of a graphene JJ embedded in a superconducting loop, which inductively couples to a co-planar transmission line (CTL) resonator. The resonant structure and supply lines are etched into NbTiN (80 nm) sputtered on an intrinsic Si/SiO_x (500 μ m/170 nm) substrate. The meandered CTL shown in Fig.1(a) is shorted on one side, and interrupted by a coupling capacitor on the other. Both of these terminations act as microwave mirrors of the opposite type, and thereby form a superconducting $\lambda/4$ -resonator with a fundamental bare resonance frequency $f_{\text{bare}} = 3.098$ GHz.

The graphene JJ, shown in Fig.1(c), is made of a van der Waals heterostructure consisting of a monolayer graphene encapsulated in hexagonal boron nitride (hBN). The lower hBN layer (47.5 nm) separates the graphene flake from the bottom graphite gate. A thermally evaporated Ti/Al (5 nm/90 nm) lead contacts the graphene from both sides [22] and encloses the junction in a loop, thus forming a graphene rf SQUID, which is inductively coupled to the current anti-node of the resonator as illustrated in Fig.1(b). The galvanic grounding of the loop defines the reference potential for the gate voltage V_{bg} applied on the bottom graphite structure. The DC current I_{flux} controls the magnetic flux Φ inside the loop and therefore tunes the external phase difference $\varphi_{\text{ext}} = 2\pi\Phi/\Phi_0$ across the rf SQUID, where $\Phi_0 = h/2e$ is the superconducting flux quantum with h being the Planck constant and e the elementary charge. Consider the Supplemental Material (SM) for details about the device fabrication [23].

In the subsequent experiment we perform reflectance measurements on the port denoted by Γ in Fig.1(a) and investigate the resonant circuit as a function of V_{bg} and I_{flux} , from which we later infer the CPR and the phase-dependent loss of the graphene JJ.

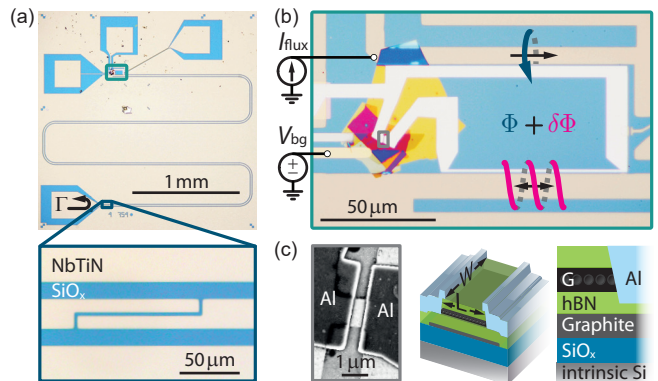


FIG. 1. Graphene rf SQUID inductively coupled to a superconducting transmission line resonator. (a) Optical image of the NbTiN $\lambda/4$ -resonator consisting of a meandered co-planar transmission line with the shorted end (current anti-node) on top, seen also at the bottom of image (b), and the open end (current node) at the bottom, shown in the zoom-in. (b) Optical image of the monolayer graphene (G) Josephson junction (JJ) embedded in an Al loop forming the rf SQUID. The DC current I_{flux} creates a flux Φ inside the loop (blue line), which allows to phase bias the junction. The inductive coupling to the resonator induces a small oscillating probe flux $\delta\Phi$ (red lines). The gate voltage V_{bg} applied on the bottom graphite sheet tunes the charge carrier density in G. (c) Scanning electron micrograph and cross-sectional schematics of the hBN-encapsulated G-JJ with Al side-contacts of width $W = 1 \mu\text{m}$ and length $L = 400$ nm.

III. REFLECTOMETRY

The coupled microwave circuit is probed by reflectometry in a dry dilution refrigerator, in which the device is surrounded by a permalloy shield. With a vector network analyzer we measure the complex reflection coefficient Γ as a function of probe frequency f and I_{flux} . We ensure a quasi-equilibrium sensing by setting the probe power to an averaged intra-cavity occupation of ~ 100 photons, which corresponds to an oscillating probe flux $\delta\Phi \approx \Phi_0/100$ inside the SQUID loop. Additionally, we tune the charge carrier density in the graphene layer by applying a gate voltage in the range $V_{\text{bg}} = [-9, 9]$ V. The conversion from V_{bg} to charge carrier density as well as the measurement scheme and the calibration of the probe power can be found in the SM [23].

The reflective response at $V_{\text{bg}} = 6$ V presented in Fig. 2 is exemplary for the whole measurement set. Clear periodic shifts of the resonance frequency f_0 as a function of I_{flux} can be observed in Fig. 2(a) and Fig. 2(b). We encounter no phase jumps and relate the external phase $\varphi_{\text{ext}} = n_{\text{odd}}\pi$ ($= n_{\text{even}}\pi$) to points of minimal (maximal) resonance frequencies [10, 14]. Besides f_0 , the resonance lineshape also changes as seen in Fig. 2(c) and Fig. 2(d) when comparing line cuts at $\varphi_{\text{ext}} = -\pi$ and $\varphi_{\text{ext}} = 0$. As we will show, both the modulation in f_0 and the altered lineshape are the consequence of the phase-dependent complex admittance of the graphene JJ.

In order to characterize the JJ from the reflective response, we fit $|\Gamma|$ and $\arg(\Gamma)$ simultaneously for each combination of V_{bg} and I_{flux} with the complex resonance curve of a loaded $\lambda/4$ -resonator expressed according to Ref. [24] as:

$$\Gamma = \left[\frac{\Gamma_{\text{min}} + 2jQ \frac{f-f_0}{f_0}}{1 + 2jQ \frac{f-f_0}{f_0}} - 1 \right] e^{j\phi} + 1. \quad (1)$$

Thus, we can deduce f_0 and assess the broadening of the resonance curve. The latter is determined by the total quality factor $Q = 1/(Q_{\text{load}}^{-1} + Q_i^{-1} + Q_c^{-1})$, which in turn, consists of three different dissipation sources: i) The inverse load quality factor Q_{load}^{-1} describes loss generated by the rf SQUID, ii) the inverse internal quality factor Q_i^{-1} describes loss inherent to the properties of the CTL and iii) the inverse coupling quality factor Q_c^{-1} describes loss to the measurement environment. Here, Q_{load}^{-1} and Q_i^{-1} are merged to an effective quality factor $Q_e = 1/(Q_{\text{load}}^{-1} + Q_i^{-1})$. Furthermore, we define $\Gamma_{\text{min}} = (Q_c - Q_e)/(Q_c + Q_e)$ and introduce the angle ϕ , which accounts for an asymmetric line shape.

The fits to Eq. 1 at $\varphi_{\text{ext}} = -\pi$ and $\varphi_{\text{ext}} = 0$, shown in Fig. 2(c) and Fig. 2(d) as solid lines, reveal an overall shift of 660 kHz in f_0 and a drastic change in Q_e , while Q_c and ϕ remain similar. At $\varphi_{\text{ext}} = -\pi$, we obtain $Q_e = 19\,400$ and $Q_c = 23\,400$; whereas at $\varphi_{\text{ext}} = 0$, we find $Q_e > 200\,000$ and $Q_c = 23\,700$. Consequently, the resonator is undercoupled ($Q_e < Q_c$) at $\varphi_{\text{ext}} = -\pi$,

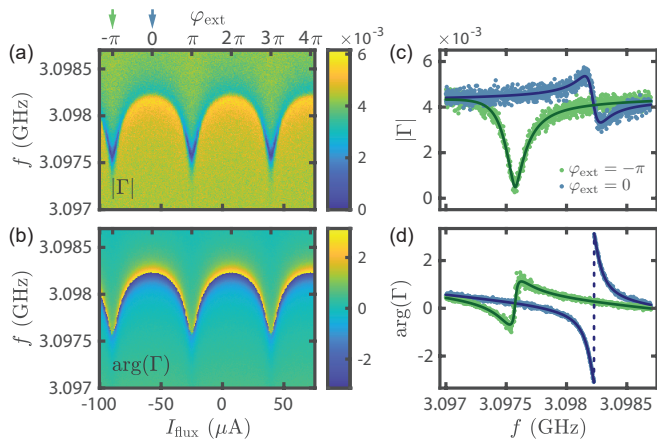


FIG. 2. Flux dependence of the reflection coefficient Γ at $V_{\text{bg}} = 6$ V. (a)-(b) Colormaps of $|\Gamma|$ and $\arg(\Gamma)$ as a function of probe frequency f and DC flux current I_{flux} . The horizontal top axis represents the conversion to the external phase φ_{ext} across the rf SQUID. (c)-(d) $|\Gamma|$ and $\arg(\Gamma)$ at $\varphi_{\text{ext}} = [-\pi, 0]$ overlaid with fits to Eq. 1 (solid lines), from which we obtain the resonance frequency f_0 , asymmetry angle ϕ , coupling quality factor Q_c and effective quality factor Q_e as listed below:

| φ_{ext} | f_0 | ϕ | Q_c | Q_e |
|------------------------|-------------|--------|--------|-----------|
| $-\pi$ | 3.09755 GHz | 0.224 | 23 400 | 19 400 |
| 0 | 3.09821 GHz | 0.235 | 23 700 | > 200 000 |

but overcoupled ($Q_e > Q_c$) at $\varphi_{\text{ext}} = 0$, which explains the distinct resonance lineshapes [25]. Since Q_i can be treated as a constant with Q_e being a lower bound, we conclude that $Q_i > 200\,000$. This large value allows us to treat the CTL as lossless ($Q_i^{-1} = 0$) such that $Q_e \approx Q_{\text{load}}$. The SM provides further insights to the resonance curve fitting [23].

The observed flux tunable microwave response in terms of f_0 and Q_{load} is the direct manifestation of phase-dependent microscopic processes in the graphene JJ [10], which will be discussed in detail in Sec. VII and Sec. VIII within the framework of ABSs. In the following section we model the electrical properties of the graphene JJ with lumped elements and explain their effect on the resonant behavior with the circuit of a loaded $\lambda/4$ -resonator.

IV. CIRCUIT MODEL

The inductively coupled rf SQUID acts as a variable load impedance Z_{load} attached to the resonator, which tunes the reflective response. We express Z_{load} according to the circuit schematic depicted in Fig. 3. The rf SQUID is modeled as a loop with self-inductance L_{loop} in series with the JJ. The mutual inductance M quantifies the coupling strength to the resonator, which is built from a CTL with characteristic impedance Z_r . The JJ itself is represented by a variable Josephson inductance L_J in parallel with a variable shunt resistance R_s . For this arrangement the load impedance terminating the resonator is detailed in the SM and reads [23]:

$$Z_{\text{load}} = \frac{\omega^2 M^2}{j\omega L_{\text{loop}} + (G_s + jB_J)^{-1}}, \quad (2)$$

where $\omega = 2\pi f$ is the angular frequency, $G_s = 1/R_s$ is the shunt conductance and $B_J = -1/(\omega L_J)$ is the susceptance. Note that $Y = G_s + jB_J$ is the complex admittance of the JJ.

The influence of Z_{load} on the $\lambda/4$ -resonator is twofold: First, the imaginary part of Z_{load} causes a shift of the resonance frequency as derived in the SM [23]

$$\delta f_0 = f_0 - f_{\text{bare}} = -\frac{2}{\pi Z_r} \text{Im}(Z_{\text{load}}) f_{\text{bare}}, \quad (3)$$

with respect to the unloaded resonance frequency f_{bare} . Second, the real part of Z_{load} gives rise to dissipation in the resonant circuit, which can be expressed according to the derivations presented in the SM as [23]

$$Q_{\text{load}} = \frac{\pi Z_r}{4 \text{Re}(Z_{\text{load}})}. \quad (4)$$

From Eq. 2 one recognizes, that the junction variables, G_s and B_J affect both $\text{Re}(Z_{\text{load}})$ and $\text{Im}(Z_{\text{load}})$. Consequently, δf_0 and Q_{load} would need to be considered simultaneously to evaluate them. However, it turns out that, due to the obtained relatively large Q_{load} values,

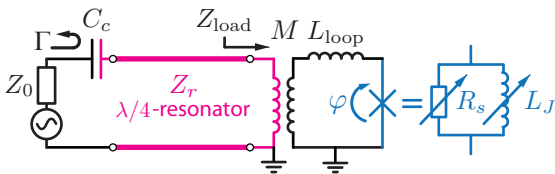


FIG. 3. Circuit schematic of a rf SQUID coupled to a $\lambda/4$ resonator. The resonator couples inductively to the rf SQUID with strength M and connects to the reflectometry setup via capacitance C_c . The rf SQUID is modeled as a loop with self-inductance L_{loop} in series with the JJ, which in turn, is modeled as a variable Josephson inductance L_J in parallel with a variable shunt resistance R_s . This forms a variable load impedance Z_{load} , which tunes the reflective response Γ .

one is allowed to set $G_s \rightarrow 0$ in Eq. 3, which simplifies the relation as shown in the SM to [23]

$$\delta f_0 \approx \frac{8}{\pi^2} \frac{M^2}{L_p (L_J + L_{\text{loop}})} f_{\text{bare}}, \quad (5)$$

where L_p is the parallel LC -equivalent inductance of the $\lambda/4$ -resonator. This means that the shift of the resonance frequency mainly originates from the Josephson inductance L_J , whereas the broadening of the resonance originates from the dissipation in the JJ specified by the shunt conductance G_s .

Since the inverse Josephson inductance is a measure of the change in the supercurrent $I_s(\varphi)$ with respect to the phase φ across the junction [6]

$$L_J(\varphi)^{-1} = \frac{2\pi}{\Phi_0} \frac{\partial I_s(\varphi)}{\partial \varphi}, \quad (6)$$

we can express the resonance frequency shift and the behavior of $L_J(\varphi)$ with the current-phase relation (CPR).

In order to quantify the CPR and G_s from the resonator response, we perform finite-element simulations [26] based on the device geometry, to acquire $L_{\text{loop}} = 211$ pH and $M = 30.83$ pH. Moreover, we find $Z_r = 69.5 \Omega$ from the aspect ratios of the CTL [27] in combination with the resonant behavior of the circuit and deduce $L_p = 4.55$ nH. The evaluation of Z_r and L_p can be found in the SM [23].

V. CURRENT-PHASE RELATION

In this section we extract the CPR by fitting the periodic shift of the resonance frequency under consideration of self-screening effects. The coupling strength between the superconducting leads is determined by the Cooper pair transmission probability and defines the shape of the CPR. For small coupling or low transmission probability the CPR is sinusoidal, whereas the CPR becomes forward-skewed for increased coupling. Due to the semiconducting properties in graphene JJs, the coupling strength and therefore the CPR skewness can be

tuned with the gate voltage [20, 28–31]. To capture the non-sinusoidal behavior, we express the CPR as Fourier series [32]

$$I_s(\varphi) = \sum_k (-1)^{k-1} A_k \sin(k\varphi), \quad (7)$$

with k being the harmonic order and A_k the corresponding amplitude.

To extract the CPR from the measured resonance frequency modulations, we need to relate the external phase φ_{ext} to the phase difference φ across the JJ. This is not straightforward, since if a supercurrent flows within the rf SQUID, there is a phase drop over the loop inductance L_{loop} in addition to the phase drop over the JJ, which leads to a non-linear relation between the internal phase φ and the external phase φ_{ext} – known as the screening effect [33]:

$$\varphi = \varphi_{\text{ext}} - \frac{2\pi}{\Phi_0} L_{\text{loop}} I_s(\varphi). \quad (8)$$

Here, we obtain the CPR for each gate voltage by solving the set of equations Eqs. 5-8 in a self-consistent way by using an iterative fitting method. The basis for this method is the resonance frequency shift as a function of φ_{ext} , which is presented for the entire gate range in Fig. 4(a). At each fitting iteration we include Fourier amplitudes A_k up to the 10th-harmonic and allow for small changes in f_{bare} . Details about the method can be found in the SM [23].

In Fig. 4(b) we illustrate the effect of screening by comparing δf_0 as a function of φ and φ_{ext} , respectively – for the example at $V_{\text{bg}} = 6$ V. The corresponding CPRs, deduced from fitting the modulations in δf_0 with respect to phase, shown as solid lines in Fig. 4(b), are presented in Fig. 4(c). The screening consideration causes a distortion of the phase around π as indicated by arrows. Omitting this effect results in an apparent enhancement of the skewness [34]. Even after correcting for screening, we find a substantially forward-skewed CPR, visualized by the comparison with a sinusoidal behavior. Although screening effects are small in this case, we emphasize that they can have a significant impact on the evaluated skewness, especially for large I_s and L_{loop} .

In Fig. 4(d) we map the extracted CPR as a function of V_{bg} . The smallest CPR amplitude is found at $V_{\text{bg}} = -0.44$ V, which we attribute to the charge neutrality point (CNP) of graphene. Here, resonance frequency modulations of only ± 10 kHz can still be clearly resolved as seen in Fig. 4(e), which demonstrates the sensitivity of the microwave circuit. The CPR at the CNP, shown in Fig. 4(f), is slightly skewed and has a maximal supercurrent of $I_c = 6.3$ nA.

In the following, we quantify the CPR and its skewness by two commonly used ways: i) by the skewness parameter $S = (2\varphi_{\text{max}}/\pi) - 1$, where φ_{max} is the phase maximizing the CPR to the critical current I_c [29], and ii) by directly providing the set of Fourier amplitudes A_k [32].

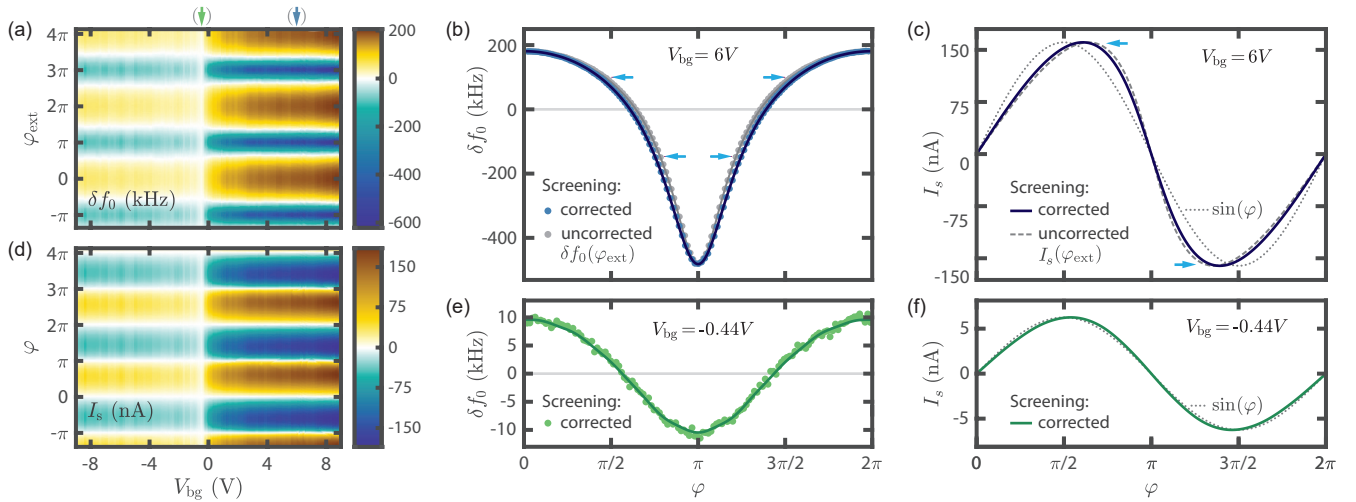


FIG. 4. Evaluation of the CPR. (a) Colormap of the resonance frequency shift $\delta f_0 = f_0 - f_{\text{bare}}$ with $f_{\text{bare}} = 3.098$ GHz as a function of gate voltage V_{bg} and external phase φ_{ext} . (b) δf_0 at $V_{\text{bg}} = 6$ V as a function of φ and φ_{ext} , respectively overlaid with the fits to Eq. 5 (solid lines), from which the CPR is deduced. (c) Presents the CPR at $V_{\text{bg}} = 6$ V, corrected for the self-screening of the SQUID (blue) and uncorrected (dashed), in comparison with the sine function (dotted). In (b)-(c) arrows illustrate the correction introduced by the non-linear mapping from φ_{ext} to φ . (d) Corrected CPR inferred from (a) as a function of V_{bg} . (e) δf_0 at the charge neutrality point ($V_{\text{bg}} = -0.44$ V) as a function of φ overlaid with the fit and in (f) the corresponding CPR.

The latter description is more precise, since it captures the entire CPR lineshape, whereas the S -parameter together with I_c do not uniquely characterize the CPR, but are more intuitive.

In Fig. 5 we employ both of these characterizations to illustrate the gate dependence of the CPR. We observe a rapid enhancement of I_c up to ~ 200 nA for gating towards positive voltages (n -doped), whereas towards negative voltages (p -doped) the increase is weaker and reaches only ~ 50 nA as seen in Fig. 5(a). Because A_1 closely follows I_c , the CPR is mainly determined by the 2π -periodic sinusoidal contribution for all V_{bg} . However, the small additions from higher harmonics lead to a forward-skewed CPR. From Fig. 5(b) it appears that the skewness saturates in both doping regimes with a slight reduction around the CNP. For the n -doped side, the skewness saturates around $S \approx 0.22$, whereas on the p -doped side the skewness is less pronounced, saturating around $S \approx 0.12$. The ratios A_k/A_1 follow the same trend.

The asymmetric behavior in I_c and S with respect to V_{bg} are attributed to the presence of n' -doped contact regions inducing additional scattering potentials. The JJ is therefore more transparent in the $n'n'n'$ -situation compared to the $n'pn'$ -case [29, 35]. We speculate that the minimal skewness of $S \approx 0.05$ close to the CNP originates from the formation of electron-hole puddles [36] in the graphene flake, which further enhance the scattering probability.

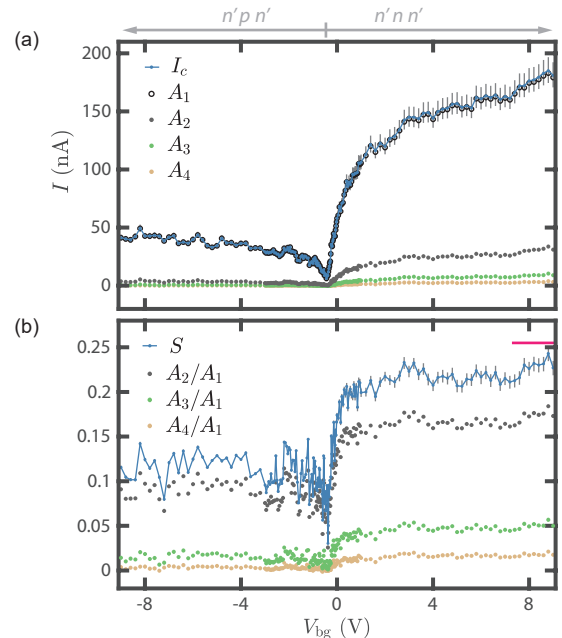


FIG. 5. Characteristics of the CPR as function of gate voltage V_{bg} . The step size in V_{bg} is reduced close to the CNP ($V_{\text{bg}} = -0.44$ V). (a) Critical current I_c and Fourier amplitudes A_k . (b) Skewness parameter S and ratios A_k/A_1 . The theoretical skewness value for a short, diffusive system under ideal conditions $S = 0.255$ is illustrated with the pink mark. (a)-(b) Systematic error bars in I_c and S are generated by modifying M by $\pm 3\%$ and L_{loop} by $\pm 5\%$ in the CPR evaluation. The amplitudes A_k for $k \geq 5$ are negligibly small and omitted in the figures.

VI. PHASE-DEPENDENT LOSS

Having extracted the CPR from the resonance frequency shift, we now deduce the phase-dependent dissipative part of the graphene JJ; namely, the shunt conductance G_s . We can infer G_s from Eq. 4, in which we express the susceptance B_J with the CPR according to Eq. 6 and make use of Q_{load} obtained from the reflectance curve analysis presented in Sec. III.

From Fig. 6(a), we observe that around the 0-points ($\varphi = n_{\text{even}}\pi$) the dissipation in the microwave circuit stemming from the rf SQUID is minor ($Q_{\text{load}} > 200\,000$) for all V_{bg} . However, at the π -points ($\varphi = n_{\text{odd}}\pi$), the dissipation becomes significantly larger and gate dependent with a minimal quality factor of $Q_{\text{load}} \approx 9800$.

This behavior is reflected in G_s , which is mapped in Fig. 6(b) as a function of V_{bg} and φ . Around the 0-points, we deduce low conductance values $G_s \leq 0.1 \text{ m}\Omega^{-1}$, which refers to weak dissipation according to the parallel junction circuit model used here. In contrast, at the π -points, a pronounced Lorentzian-shaped dissipation peak develops, as seen in Fig. 6(c). The dissipation onsets are located symmetrically around the π -points and are weakly gate dependent. On the other hand, the peak heights are strongly influenced by V_{bg} and reach a maximal value of $G_s \approx 10 \text{ m}\Omega^{-1}$ at large n -doping. Although the amplitude of the peak appears to fluctuate as a function of V_{bg} , the height replicates for the three different π -points measured here, as illustrated in Fig. 6(d). This demonstrates the stability of the gate-tunable potential landscape in graphene. In order to explain the dissipative response of the JJ, the underlying phase-dependent transport processes need to be considered, which are discussed in the next section.

VII. THEORY OF ANDREEV BOUND STATES

In the following we relate the CPR and the phase-dependent dissipation to the microscopic concept of Andreev bound states (ABSs) formed within the JJ.

Coherent Andreev reflections of quasiparticles at the graphene-superconductor interfaces lead to the formation of ABSs [37]. These quasiparticle states transfer Cooper pairs across the junction in form of counter propagating electron-hole pairs [38]. Due to the electron-hole symmetry, the ABSs come in pairs; one state has negative energy $E_n^- \leq 0$ and the other has positive energy $E_n^+ = -E_n^-$, where n denotes a specific transport channel. The spectral gap δE quantifies the minimal transition energy between states with negative and states with positive energies. Each occupied state carries current proportional to the derivative of its energy with respect to phase. The sum over the set of all channels defines the total supercurrent [39], which can be expressed as

$$I_s(\varphi) = \frac{2\pi}{\Phi_0} \sum_n f(E_n^\pm) \frac{\partial E_n^\pm}{\partial \varphi}, \quad (9)$$

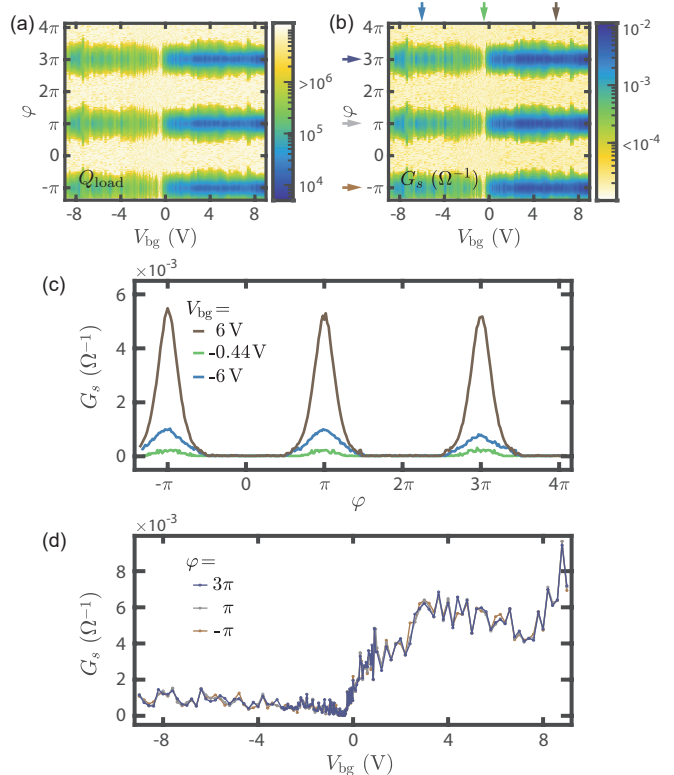


FIG. 6. Evaluation of the shunt conductance G_s . (a) The load quality factor Q_{load} in logarithmic scale as a function of V_{bg} and φ , deduced from resonance curve fittings. (b) G_s in logarithmic scale obtained by using Eq. 4 with Q_{load} and the CPR results. (c) Phase dependence of G_s for different gate voltages. (d) Gate dependence of G_s for phase biasing conditions $\varphi = n_{\text{odd}}\pi$.

where $f(E_n^\pm)$ is a functional describing the occupation probability of the n^{th} ABS. In equilibrium the functional is given by the Fermi-Dirac distribution.

At zero temperature and in the absence of photons, all ABSs with negative energies are occupied ($f(E_n^-) = 1$), whereas all ABSs with positive energies are empty ($f(E_n^+) = 0$). In this situation the system is in the ground state and the occupation of the ABS spectrum is constant. Therefore the supercurrent I_s is free of any fluctuations. By virtue of the fluctuation-dissipation theorem, [40] there is no dissipation and the effective junction shunt conductance assumes $G_s \rightarrow 0$.

When finite electronic temperatures T and/or the absorption of photons from the electromagnetic environment are considered, the situation becomes different; thermal activation and/or microwave-induced transitions will drive the system out of the ground state. The excitation-relaxation dynamics give rise to fluctuations in the ABS population, and correspondingly, in the supercurrent as well. Consequently, there is dissipation and a finite shunt conductance G_s appears [8]. When the spectral gap closes ($\delta E \rightarrow 0$) already small temperatures T and small photon energies hf will trigger fluctuations.

We note that the fluctuations are determined by the temperature, the photon absorption and emission rates and as well by the relaxation time τ_{rel} of a non-thermal distribution towards a thermal one, which we express in the following as the energy $\gamma = \hbar/(2\tau_{\text{rel}})$. In conclusion, this means that in general, both the inductive and dissipative part of a JJ depend on the ABS spectrum and the population dynamics within this spectrum.

Inherent to wide junctions – like the graphene JJ investigated here – is that there are various possible transport channels leading to many ABSs and hence to a dense ABS spectrum [41]. The phase dependence of the ABS spectrum is determined by the geometry of the JJ and its material properties, i.e. the superconducting gap Δ in the leads and the inverse transport time in the normal region that relates to the Thouless energy E_T . An important characteristic of JJs is whether they are in the ‘short’ or ‘long’ junction limit. The former case is realized when $E_T \gg \Delta$, while the latter holds in the opposite limit. The condition for the short junction limit can also be expressed as the coherence length ξ being longer than the junction length L . Since this quantity for similar devices is reported to be $\xi \approx 500$ nm [41, 42] and the junction under investigation has a length $L = 400$ nm, the condition for the short junction limit seems reasonably valid.

For JJs in the short junction limit the ABS energies are given by $E_n^\pm(\varphi) = \pm\Delta\sqrt{1 - \tau_n \sin^2(\varphi/2)}$, where τ_n is the transmission probability of the n^{th} channel. Thus, the ABS spectrum strongly depends on the transparency distribution, which further defines the transport regime. For diffusive transport the transmission coefficients are continuously distributed following Dorokhov’s bimodal distribution [43], which describes that there are many channels with low transmission ($\tau_n \rightarrow 0$), but also many with high transmission probabilities ($\tau_n \rightarrow 1$). Consequently, a dense ABS spectrum emerges as illustrated in Fig. 7(a) with a spectral gap $\delta E = 2\Delta|\cos(\varphi/2)|$ that closes ($\delta E \rightarrow 0$) towards the π -points and maximally opens ($\delta E = 2\Delta$) towards the 0-points. In the following we assume predominant diffusive transport in the graphene JJ investigated here, which is supported by multiple observations: i) the small discrepancy between the experimentally determined skewness at large n -doping ($S \approx 0.22$) and the one predicted theoretically ($S = 0.255$) [44], ii) the lack of Fabry-Pérot oscillations in the gate dependence of the CPR presented in Fig. 5 indicates suppressed ballistic transport [29], and iii) the randomly evolving shunt conductance G_s seen in Fig. 6 hints at universal conductance fluctuations, which are expected for diffusive systems. We believe that here the diffusive character of the device is stemming from scattering processes at the graphene edges, which are significant due to a small width to length ratio ($W/L \approx 2$), and hence reduce the amount of ballistic channels.

In order to evaluate the dynamics of the ABS spectrum described above and translate it to lumped element quantities, we make use of theoretical works that predict the phase-dependent linear microwave response in terms of

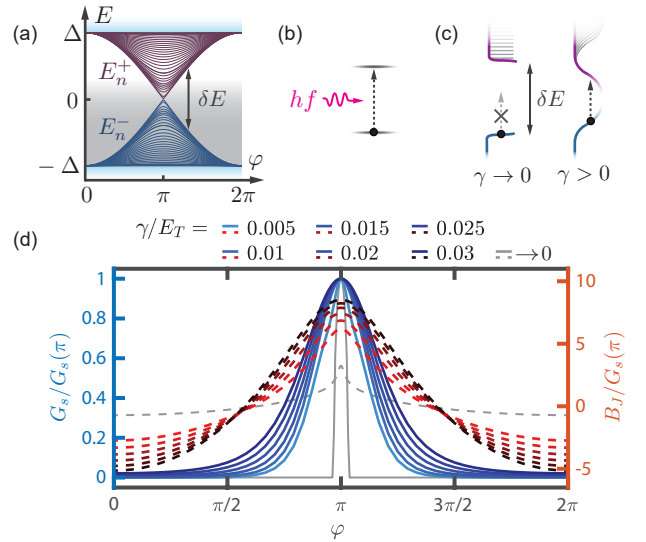


FIG. 7. ABS spectrum and theoretical microwave response for a short, diffusive JJ. (a) Spectrum of a short JJ with multiple channels of different transparencies. (b) Microwave-induced transitions between states triggered by the absorption of a photon with energy hf . (c) The finite lifetime of states described by the relaxation rate γ causes a spectral broadening of the ABS energies and hence blurs the transition condition. (d) Theoretically predicted dissipative and inductive response: G_s (blue, left axis) and B_J (red, right axis) normalized by the conductance value at $\varphi = \pi$ as function φ for different γ/E_T ratios. The normalization values for increasing γ/E_T read: $G_s(\pi)/G_N = 45, 11, 8.6, 7, 5.9, 5, 4.4$, where G_N is the normal state conductance. Here: $\Delta/E_T = 0.1$, $hf/E_T = 0.01$ and $kT/E_T = 0.008$.

the susceptance B_J and the shunt conductance G_s [3, 4]. For the theoretical analysis we consider a diffusive multi-channel JJ in the short junction limit at finite temperature coupled to a photonic environment of energy hf . Note that in the experiment the photonic environment is provided by the driven microwave resonator.

First we consider the case of long-lived excitations ($\gamma \rightarrow 0$), for which we find a sharp onset in $G_s(\varphi)$ as seen by the solid gray line in Fig. 7(d). The dissipation occurs in the phase range, where the spectral gap becomes smaller than the excitation energy $\delta E \leq hf$, thus allowing microwave-induced cross-gap transitions. The width and the height of the dissipation peak depends on characteristic energy scales, which are denoted in the figure caption. It is worth mentioning that not only transitions across the gap lead to dissipation; all possible absorption processes, including intra-band excitations $E_n^+ \rightarrow E_m^+$, contribute to it, whereas the transition probability scales according to Fermi’s Golden rule with the available density of states [13]. Fig. 7(b) depicts a microwave-induced transition of a quasiparticle from an arbitrary initial state to an available final state. The fact that the ABSs have a finite lifetime causes a spectral broadening of the energies. This results in a blurring of the transition condition ($\delta E \leq hf$) as sketched in Fig. 7(c). Therefore, increasing

γ , i.e., shortening the lifetime, broadens the dissipation peak as seen by the blue lines in Fig. 7(d). Importantly, the lifetime broadening also affects the susceptance, in particular the phase conditions for $B_J = 0$ shift away from the π -point, which is equivalent to a reduction of the CPR skewness. Note that B_J for $\gamma \rightarrow 0$ shown in dashed gray appears different, because it is rescaled with a large conductance value $G_s(\pi)$. A representation of Fig. 7(d) without normalization is shown in the SM [23].

The influence of temperature on the microwave response is theoretically discussed, and together with experimental results, presented in the SM [23].

In short, environmental perturbations, namely, temperature and electromagnetic irradiation, cause dynamical variations in the population of ABS spectra on the timescale of the non-equilibrium occupation lifetime, which influence the susceptance B_J likewise the CPR and give rise to dissipation captured by the shunt conductance G_s .

VIII. COMPARISON WITH THEORY

Finally, we compare the experimental results of the graphene junction with theoretical predictions based on the assumption of a short, diffusive multi-channel JJ.

One theoretical prediction, which was not explicitly pointed out above, is that the inductive and dissipative response (B_J, G_s) scale linearly with the normal state conductance G_N [3, 4], which is tunable with the gate voltage in our experiment. From Fig. 8(a) one can verify this relation, since the relation between the experimentally deduced values of the susceptance B_J and conductance G_s obtained at $\varphi = \pi$ for all different V_{bg} – clearly follows a linear trend. Furthermore, the ratio B_J/G_s is the inverse loss tangent describing the quality of the Josephson inductance [14], where a larger ratio implies a more ideal behavior of the inductance. We attribute the cone-shaped spread in Fig. 8(a) around the mean ratio ($\langle B_J(\pi)/G_s(\pi) \rangle \approx 7$) to altered ABS spectra and modified relaxation dynamics at different gate voltages.

In the next step, we search for the best match between the theoretically predicted and the experimentally deduced phase-dependent microwave response by considering both the inductive and the dissipative properties of the JJ. To this end, we numerically generate sets of B_J and G_s with different characteristic parameters. In particular, we vary the ratios kT/E_T and γ/E_T to account for a finite electronic temperature and to capture the effect of lifetime broadening. We have fixed the Thouless energy to $E_T = 10\Delta$ and the photon energy to $hf = \Delta/10$: the first condition ensures the short junction limit, whereas the second one compares favourably well to the expected experimental relation between the photon energy of the resonator and the superconducting gap of the contact material.

In Fig. 8(b) we compare the normalized theoretical and experimental values for $V_{\text{bg}} = -6\text{ V}$, whereas in Fig. 8(c)

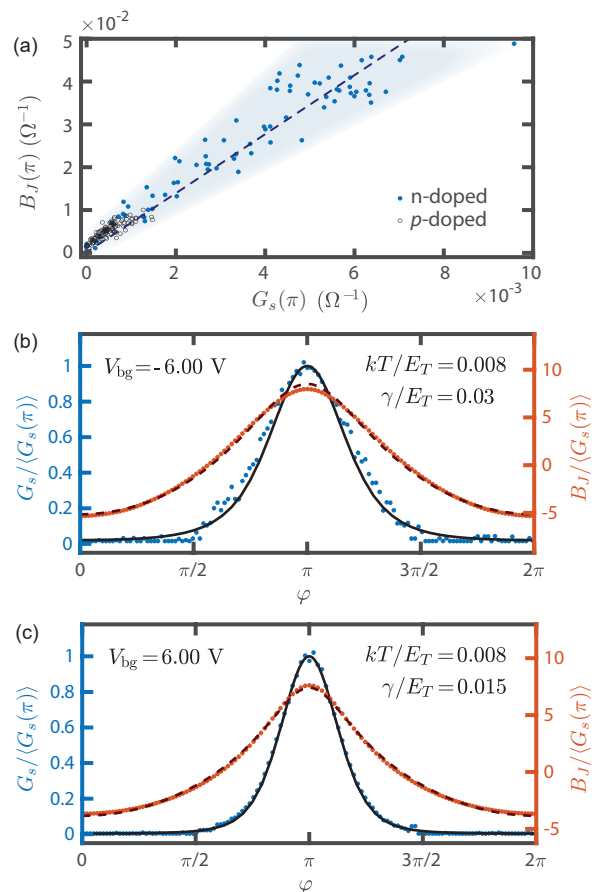


FIG. 8. Experimental observations in comparison with theoretical predictions for a short, diffusive JJ. (a) Experimentally obtained susceptance B_J versus shunt conductance G_s at $\varphi = \pi$ follows a mean ratio of ~ 7 indicated with the dashed line. (b)-(c) Normalized measured G_s (dotted blue, left axis) and B_J (dotted red, right axis) overlaid with the normalized theoretical predictions for G_s (solid) and B_J (dashed), for which $\Delta/E_T = 0.1$ and $hf/E_T = 0.01$ are fixed, but kT/E_T and γ/E_T are variable. The best fitting parameter ratios are indicated. For $V_{\text{bg}} = -6\text{ V}$ (6 V) the normalizations read $\langle G_s(\pi) \rangle = 0.98\text{ m}\Omega^{-1}$ ($5.23\text{ m}\Omega^{-1}$) for the experimental traces and for the theoretical traces $G_s(\pi)/G_N = 4.4$ (7).

we perform the comparison for $V_{\text{bg}} = 6\text{ V}$. The experimental values G_s (blue dots) and B_J (red dots) are normalized with the shunt conductance at $\varphi = \pi$, denoted by $\langle G_s(\pi) \rangle$ [45]. Close overlap between theory and experiment can be found for both gate voltages with the same temperature ($kT/E_T = 0.008$), but distinct relaxation rates γ .

At $V_{\text{bg}} = -6\text{ V}$ we observe differences between the model and the experimental data even with the best match ($\gamma/E_T = 0.03$). This is especially evident at the flanks of the dissipation peak and the susceptance at the π -point. We attribute this mismatch to an inappropriate choice of transport regime for this gate voltage, because here the additional pn' -junctions at the interfaces effectively elongate the quasiparticle trajectories. Con-

sequently, the JJ tends to be in the long-junction limit causing a compression of the ABS spectrum.

On the other hand, we stress that we observe striking agreements between the theoretical predictions with $\gamma/E_T = 0.015$ and the experimental data at $V_{bg} = 6$ V. Apparently, the model of a short, diffusive junction reproduces simultaneously the inductive and dissipative response of the graphene JJ for this doping configuration. By evaluating the best fitting ratios $kT/hf = 0.8$ and $\gamma/hf = 1.5$ with the resonance frequency $f = 3.098$ GHz, we deduce an electronic temperature $T = 120$ mK and obtain a relaxation time $\tau_{rel} = 17$ ps. A similar equilibration time ($\tau_{rel} = 7$ ps) is reported for an equivalent short, diffusive Al-graphene JJ probed at mK temperatures and large n -dopings [46]. We stress that the ABS spectrum of a short, diffusive junction might not be the only spectrum, which in a similar theoretical model could reproduce the experimentally observed response. In particular, in a wide JJ the ABS spectrum can be built from quasiparticles with long and short trajectories leading to more complex ABS structures than discussed above [41].

IX. CONCLUSION

We have measured the reflective response of a microwave resonator inductively coupled to a graphene-based rf SQUID as a function of flux-bias and charge carrier density. We developed a concise circuit model to infer the CPR and the phase-dependent dissipation of the graphene JJ from the changes in the resonance frequency and broadening. We hereby obtain the full complex admittance of the junction, which is the key parameter to design Josephson microwave circuits.

Our comprehensive investigation demonstrates the impact of the environment on the performance of JJs in terms of finite temperature and microwave photons. If the environment provides energies larger than the spectral gap, short-lived excitations appear in the ABS spectrum, which induce fluctuations in the supercurrent leading to dissipation. The comparison between the experimentally deduced microwave response at high electron density and the one predicted by theory for a short and diffusive junction model, yields striking agreement, from which we deduce a relaxation time of 17 ps. This fast thermal relaxation makes graphene-based JJs unique candidates for highly sensitive and fast bolometers [16, 17, 47].

Furthermore, the device architecture and measurement

protocols presented in this work are well-suited to explore the fundamental properties of other JJs, such as junctions made of 2D/3D topological insulators or Dirac and Weyl semimetals [48]. Particularly, the topological nature of these JJs can be probed, because it is predicted that they host ABS states that cross at the π -points but possess opposite parities, meaning that microwave-induced transitions across the gap are prohibited [49]. As a consequence, it is expected that the dissipative character of topological JJs is distinctly different from trivial ones [50–52].

ACKNOWLEDGMENTS

We thank S. Dehm for technical support in the nanofabrication facility at KIT. We are grateful for discussions about general properties of 2D Josephson junction with A. Kononov and P. Karnatak. This research was supported by the Swiss National Science Foundation through a) grants No 172638 and 192027, b) the National Centre of Competence in Research Quantum Science and Technology (QSIT), and c) the QuantEra project SuperTop; the János Bolyai Research Scholarship of the Hungarian Academy of Sciences, the National Research Development and Innovation Office (NKFIH) through the OTKA Grants FK 132146 and NN127903 (FlagERA Topograph), and the National Research, Development and Innovation Fund of Hungary within the Quantum Technology National Excellence Program (Project Nr. 2017-1.2.1-NKP-2017-00001), the Quantum Information National Laboratory of Hungary and the ÚNKP-20-5 New National Excellence Program. We further acknowledge funding from the European Union’s Horizon 2020 research and innovation programme, specifically a) from the European Research Council (ERC) grant agreement No 787414, ERC-Adv TopSupra, and b) grant agreement No 828948, FET-open project AndQC. This work was partly supported by Helmholtz society through program STN and the DFG via the projects DA 1280/3-1. K. Watanabe and T. Taniguchi acknowledge support from the Elemental Strategy Initiative conducted by the MEXT, Japan, Grant Number JPMXP0112101001, JSPS KAKENHI Grant Number JP20H00354 and the CREST(JPMJCR15F3), JST.

All raw- and metadata in this publication are available in numerical form together with the processing codes at DOI: 10.5281/zenodo.4479896.

-
- [1] I. O. Kulik, Macroscopic quantization and the proximity effect in S-N-S junctions, *Sov. Phys. JETP* **30**, 944 (1970).
 - [2] A. A. Golubov, M. Y. Kupriyanov, and E. Il’ichev, The current-phase relation in Josephson junctions, *Rev. Mod. Phys.* **76**, 411 (2004).
 - [3] P. Virtanen, F. S. Bergeret, J. C. Cuevas, and T. T. Heikkilä, Linear ac response of diffusive SNS junctions, *Phys. Rev. B* **83**, 144514 (2011).
 - [4] F. Kos, S. E. Nigg, and L. I. Glazman, Frequency-dependent admittance of a short superconducting weak link, *Phys. Rev. B* **87**, 174521 (2013).

- [5] P. F. Bagwell, Suppression of the Josephson current through a narrow, mesoscopic, semiconductor channel by a single impurity, *Phys. Rev. B* **46**, 12573 (1992).
- [6] A. Paila, D. Gunnarsson, J. Sarkar, M. A. Sillanpää, and P. J. Hakonen, Current-phase relation and Josephson inductance in a superconducting Cooper-pair transistor, *Phys. Rev. B* **80**, 144520 (2009).
- [7] D. Averin and H. T. Imam, Supercurrent Noise in Quantum Point Contacts, *Phys. Rev. Lett.* **76**, 3814 (1996).
- [8] A. Martín-Rodero, A. Levy Yeyati, and F. J. García-Vidal, Thermal noise in superconducting quantum point contacts, *Phys. Rev. B* **53**, R8891 (1996).
- [9] B. Dassonneville, A. Murani, M. Ferrier, S. Guéron, and H. Bouchiat, Coherence-enhanced phase-dependent dissipation in long SNS Josephson junctions: Revealing Andreev bound state dynamics, *Phys. Rev. B* **97**, 184505 (2018).
- [10] F. Chiodi, M. Ferrier, K. Tikhonov, P. Virtanen, T. T. Heikkilä, M. Feigelman, S. Guéron, and H. Bouchiat, Probing the dynamics of Andreev states in a coherent Normal/Superconducting ring, *Sci. Rep.* **1**, 3 (2011).
- [11] M. Ferrier, B. Dassonneville, S. Guéron, and H. Bouchiat, Phase-dependent Andreev spectrum in a diffusive SNS junction: Static and dynamic current response, *Phys. Rev. B* **88**, 174505 (2013).
- [12] B. Dassonneville, M. Ferrier, S. Guéron, and H. Bouchiat, Dissipation and Supercurrent Fluctuations in a Diffusive Normal-Metal-Superconductor Ring, *Phys. Rev. Lett.* **110**, 217001 (2013).
- [13] Z. Dou, T. Wakamura, P. Virtanen, N.-J. Wu, R. Deblock, S. Autier-Laurent, K. Watanabe, T. Taniguchi, S. Guéron, H. Bouchiat, and M. Ferrier, Microwave photoassisted dissipation and supercurrent of a phase-biased graphene-superconductor ring, *Phys. Rev. Res.* **3**, L032009 (2021).
- [14] R. E. Lake, J. Govenius, R. Kokkonen, K. Y. Tan, M. Partanen, P. Virtanen, and M. Möttönen, Microwave Admittance of Gold-Palladium Nanowires with Proximity-Induced Superconductivity, *Adv. Electron. Mater.* **3**, 1600227 (2017).
- [15] R. Aguado, A perspective on semiconductor-based superconducting qubits, *Appl. Phys. Lett.* **117**, 240501 (2020).
- [16] G.-H. Lee, D. K. Efetov, W. Jung, L. Ranzani, E. D. Walsh, T. A. Ohki, T. Taniguchi, K. Watanabe, P. Kim, D. Englund, and K. C. Fong, Graphene-based Josephson junction microwave bolometer, *Nature* **586**, 42 (2020).
- [17] R. Kokkonen, J.-P. Girard, D. Hazra, A. Laitinen, J. Govenius, R. E. Lake, I. Sallinen, V. Vesterinen, M. Partanen, J. Y. Tan, K. W. Chan, K. Y. Tan, P. Hakonen, and M. Möttönen, Bolometer operating at the threshold for circuit quantum electrodynamics, *Nature* **586**, 47 (2020).
- [18] J. G. Kroll, W. Uilhoorn, K. L. van der Enden, D. de Jong, K. Watanabe, T. Taniguchi, S. Goswami, M. C. Cassidy, and L. P. Kouwenhoven, Magnetic field compatible circuit quantum electrodynamics with graphene Josephson junctions, *Nat. Commun.* **9**, 4615 (2018).
- [19] J. I.-J. Wang, D. Rodan-Legrain, L. Bretheau, D. L. Campbell, B. Kannan, D. Kim, M. Kjaergaard, P. Krantz, G. O. Samach, F. Yan, J. L. Yoder, K. Watanabe, T. Taniguchi, T. P. Orlando, S. Gustavsson, P. Jarillo-Herrero, and W. D. Oliver, Coherent control of a hybrid superconducting circuit made with graphene-based van der Waals heterostructures, *Nat. Nanotechnol.* **14**, 120 (2019).
- [20] F. E. Schmidt, M. D. Jenkins, K. Watanabe, T. Taniguchi, and G. A. Steele, A ballistic graphene superconducting microwave circuit, *Nat. Commun.* **9**, 4069 (2018).
- [21] F. E. Schmidt, M. D. Jenkins, K. Watanabe, T. Taniguchi, and G. A. Steele, Probing the current-phase relation of graphene Josephson junctions using microwave measurements (2020), arXiv:2007.09795 [cond-mat.mes-hall].
- [22] L. Wang, I. Meric, P. Y. Huang, Q. Gao, Y. Gao, H. Tran, T. Taniguchi, K. Watanabe, L. M. Campos, D. A. Muller, J. Guo, P. Kim, J. Hone, K. L. Shepard, and C. R. Dean, One-Dimensional Electrical Contact to a Two-Dimensional Material, *Science* **342**, 614 (2013).
- [23] See Supplemental Material for details about the device fabrication (Sec. SI), measurement scheme and calibrations (Sec. SII, SIII and SX), procedures for fitting the resonance curve (Sec. SIV), derivations and validity proof for the formulas relating the resonant behavior to the electrical properties of the JJ (Sec. SV-SVIII), iterative fitting routine to correct for screening (Sec. SIX) and theoretical as well as experimental results as a function of temperature (Sec. SXI).
- [24] M. S. Khalil, M. J. A. Stoutimore, F. C. Wellstood, and K. D. Osborn, An analysis method for asymmetric resonator transmission applied to superconducting devices, *J. Appl. Phys.* **111**, 054510 (2012).
- [25] M. Göppl, A. Fragner, M. Baur, R. Bianchetti, S. Filipp, J. M. Fink, P. J. Leek, G. Puebla, L. Steffen, and A. Wallraff, Coplanar waveguide resonators for circuit quantum electrodynamics, *J. Appl. Phys.* **104**, 113904 (2008).
- [26] E. U. Manual, Sonnet software, Inc., Liverpool, NY, 50 (2005).
- [27] S. Gevorgian, Basic characteristics of two layered substrate coplanar waveguides, *Electron. Lett.* **30**, 1236 (1994).
- [28] C. D. English, D. R. Hamilton, C. Chialvo, I. C. Moraru, N. Mason, and D. J. Van Harlingen, Observation of non-sinusoidal current-phase relation in graphene Josephson junctions, *Phys. Rev. B* **94**, 115435 (2016).
- [29] G. Nanda, J. L. Aguilera-Servin, P. Rakyta, A. Kormányos, R. Kleiner, D. Koelle, K. Watanabe, T. Taniguchi, L. M. K. Vandersypen, and S. Goswami, Current-Phase Relation of Ballistic Graphene Josephson Junctions, *Nano Lett.* **17**, 3396 (2017).
- [30] D. I. Indolese, P. Karnatak, A. Kononov, R. Delagrè, R. Haller, L. Wang, P. Makk, K. Watanabe, T. Taniguchi, and C. Schönenberger, Compact SQUID Realized in a Double-Layer Graphene Heterostructure, *Nano Lett.* **20**, 7129 (2020).
- [31] D. A. Manjarrés, S. Gómez Páez, and W. J. Herrera, Skewness and critical current behavior in a graphene Josephson junction, *Phys. Rev. B* **101**, 064503 (2020).
- [32] E. M. Spanton, M. Deng, S. Vaitiekėnas, P. Krogstrup, J. Nygård, C. M. Marcus, and K. A. Moler, Current-phase relations of few-mode InAs nanowire Josephson junctions, *Nat. Phys.* **13**, 1177 (2017).
- [33] P. Jung, S. Butz, S. V. Shitov, and A. V. Ustinov, Low-loss tunable metamaterials using superconducting circuits with Josephson junctions, *Appl. Phys. Lett.* **102**, 062601 (2013).
- [34] F. Nichele, E. Portolés, A. Fornieri, A. M. Whiticar,

- A. C. C. Drachmann, S. Gronin, T. Wang, G. C. Gardner, C. Thomas, A. T. Hatke, M. J. Manfra, and C. M. Marcus, Relating Andreev Bound States and Supercurrents in Hybrid Josephson Junctions, *Phys. Rev. Lett.* **124**, 226801 (2020).
- [35] I. V. Borzenets, F. Amet, C. T. Ke, A. W. Draelos, M. T. Wei, A. Seredinski, K. Watanabe, T. Taniguchi, Y. Bomze, M. Yamamoto, S. Tarucha, and G. Finkelstein, Ballistic Graphene Josephson Junctions from the Short to the Long Junction Regimes, *Phys. Rev. Lett.* **117**, 237002 (2016).
- [36] J. Xue, J. Sanchez-Yamagishi, D. Bulmash, P. Jacquod, A. Deshpande, K. Watanabe, T. Taniguchi, P. Jarillo-Herrero, and B. J. LeRoy, Scanning tunnelling microscopy and spectroscopy of ultra-flat graphene on hexagonal boron nitride, *Nat. Mater.* **10**, 282 (2011).
- [37] A. F. Andreev, The thermal conductivity of the intermediate state in superconductors, *Sov. Phys. JETP* **19**, 1228 (1964).
- [38] J.-D. Pillet, C. H. L. Quay, P. Morfin, C. Bena, A. Levy Yeyati, and P. Joyez, Andreev bound states in supercurrent-carrying carbon nanotubes revealed, *Nat. Phys.* **6**, 965 (2010).
- [39] C. W. J. Beenakker, Universal limit of critical-current fluctuations in mesoscopic josephson junctions, *Phys. Rev. Lett.* **67**, 3836 (1991).
- [40] J. G. Hoffman, The fluctuation dissipation theorem, *Phys. Today* **15**, 30 (1962).
- [41] L. Bretheau, J. I.-J. Wang, R. Pisoni, K. Watanabe, T. Taniguchi, and P. Jarillo-Herrero, Tunnelling spectroscopy of Andreev states in graphene, *Nat. Phys.* **13**, 756 (2017).
- [42] C. Li, S. Guéron, A. Chepelianskii, and H. Bouchiat, Full range of proximity effect probed with superconductor/graphene/superconductor junctions, *Phys. Rev. B* **94**, 115405 (2016).
- [43] O. Dorokhov, On the coexistence of localized and extended electronic states in the metallic phase, *Solid State Commun.* **51**, 381 (1984).
- [44] The CPR of a short, diffusive junction in equilibrium can be expressed analytically, from which one obtains a skewness $S = 0.255$ at $T = 0$ [4, 53] as indicated by the pink mark in Fig. 5. The reduced skewness in the p -doped regime ($S \approx 0.12$) we assign to an overall suppression of the transmission probability due to the formation of pn' -junctions at the graphene-superconductor interfaces.
- [45] We average the three shunt conductance values closest to $\varphi = \pi$ to accommodate for scattering of the data.
- [46] J. Voutilainen, A. Fay, P. Häkkinen, J. K. Viljas, T. T. Heikkilä, and P. J. Hakonen, Energy relaxation in graphene and its measurement with supercurrent, *Phys. Rev. B* **84**, 045419 (2011).
- [47] D. K. Efetov, R.-J. Shiue, Y. Gao, B. Skinner, E. D. Walsh, H. Choi, J. Zheng, C. Tan, G. Grosso, C. Peng, J. Hone, K. C. Fong, and D. Englund, Fast thermal relaxation in cavity-coupled graphene bolometers with a Johnson noise read-out, *Nat. Nanotechnol.* **13**, 797 (2018).
- [48] A. Murani, B. Dassonneville, A. Kasumov, J. Basset, M. Ferrier, R. Deblock, S. Guéron, and H. Bouchiat, Microwave Signature of Topological Andreev level Crossings in a Bismuth-based Josephson Junction, *Phys. Rev. Lett.* **122**, 076802 (2019).
- [49] Y. Peng, F. Pientka, E. Berg, Y. Oreg, and F. von Oppen, Signatures of topological Josephson junctions, *Phys. Rev. B* **94**, 085409 (2016).
- [50] R. M. Lutchyn, J. D. Sau, and S. Das Sarma, Majorana Fermions and a Topological Phase Transition in Semiconductor-Superconductor Heterostructures, *Phys. Rev. Lett.* **105**, 077001 (2010).
- [51] O. Dmytruk, M. Trif, and P. Simon, Josephson effect in topological superconducting rings coupled to a microwave cavity, *Phys. Rev. B* **94**, 115423 (2016).
- [52] M. Trif, O. Dmytruk, H. Bouchiat, R. Aguado, and P. Simon, Dynamic current susceptibility as a probe of Majorana bound states in nanowire-based Josephson junctions, *Phys. Rev. B* **97**, 041415(R) (2018).
- [53] T. T. Heikkilä, J. Särkkä, and F. K. Wilhelm, Supercurrent-carrying density of states in diffusive mesoscopic Josephson weak links, *Phys. Rev. B* **66**, 184513 (2002).

Supplementary Material: Phase-dependent microwave response of a graphene Josephson junction

SI. FABRICATION

A. NbTiN sputtering

The NbTiN film (80 nm) is sputtered on an undoped Si/SiO₂ wafer (500 μm /170 nm) in a AJA[©] ATC Orion 8 sputtering machine using a NbTi-target (70/30 at%, 99.995% purity) and N₂ added to the Ar sputtering gas. Before deposition, following wafer cleaning steps are performed:

- 10 min sonication in deconex[©] 12 basic/DI-water solution \rightarrow flush with DI-water
- 10 min sonication in DI-water \rightarrow blow-dry
- 5 min baking at 120 °C
- 10 min sonication in acetone
- 10 min sonication in IPA \rightarrow blow-dry
- 5 min UV-ozone in UVO-Cleaner[©] Model 42-220

After inserting the wafer into the sputtering machine typical base pressures of $\sim 8 \times 10^{-9}$ Torr are achieved. We position the wafer as close as possible to the NbTi target to minimize particle scattering. Before depositing on the wafer substrate – the chamber and the NbTi-target are conditioned. During the conditioning steps a substrate shutter protects the wafer from material deposition. We pre-sputter Ti (35 sccm of Ar at 4 mTorr with (DC) 100 W for 20 min) to remove oxygen residuals in the chamber. After terminating the Ti pre-sputtering, we pump on the chamber until pressures $< 1 \times 10^{-9}$ Torr are reached, which typically takes ~ 20 min. Then we sputter NbTi+N₂ (50 sccm of Ar, 3.5 sccm of N₂ at 2 mTorr with (DC) 275 W). After 4 min of sputtering time, we open the substrate shutter to allow for deposition on the wafer – for totally 375 s, which results in a film thickness of ~ 80 nm. The N₂-flow was optimized separately to achieve a stoichiometric compound of NbTiN.

B. Resonator and graphene Josephson junction

After the sputter deposition of NbTiN – the resonator is defined, then the separately prepared van der Waals heterostructure is placed and contacted as explained in the following:

Resonator patterning: The resonant structure and supply lines in NbTiN are patterned by using positive e-beam lithography (EBL) followed by an Ar/Cl₂ reactive-ion etching-step. The meandered co-planar transmission line (TL) is designed with a central conductor width of 12 μm , a clearance of 6 μm to the surrounding ground plane and a total length of $l = 7.54$ mm. The TL is shorted to ground on one side and interrupted by a coupling capacitance on the other, which forms the $\lambda/4$ -resonator. The dimensions of the finger capacitor are aimed for providing a coupling capacitance of ~ 4 fF. From the measurement and calculations presented below we deduce for this configuration a resonance frequency $f_0 \approx 3.098$ GHz, a characteristic impedance $Z_r = 69.5 \Omega$ and a coupling capacitance $C_c = 4.7$ fF. The supply lines for the gate, flux, and pump are designed on purpose with different aspect ratios to provoke an impedance mismatch for minimizing loss channels for the resonator. For this experiment we do not make use of the pump line (upper right in Fig. 1(a) of the maintext). The fabrication details are listed below.

- Resist: AR-P[©] 671.05 (positive PMMA resist, 950k, 5% diluted in chlorobenzene)
- Coating: Spin with 6000 rpm for 40 s (ramp 4 s) \rightarrow thickness 600 nm.
- Bake: 5 min on the hot plate at 180 °C
- EBL with Zeiss[©] Supra 40: 20 kV acceleration voltage, aperture of 60 μm in high current mode and a dose of 275 $\mu\text{C}/\text{cm}^2$
- Resist development: MIBK/IPA 1:3 at room temperature for 60 s. The development is followed by 10 s in IPA \rightarrow blow-dry
- O₂-plasma in Oxford[©] Plasmalab 80 Plus: 2 min with 30 W and 16 sccm of O₂-flow at 250 mTorr

- NbTiN etching in Sentech[©] SI500: 1 Pa, ICP power 100 W, RF power 125 W with 40 sccm of Cl₂ and 25 sccm of Ar for 40 s; etch rate ~ 3 nm/s
- Lift-off: 1 h in acetone at 50 °C followed by sonication and rising with IPA \rightarrow blow-dry

Preparation of the graphene van der Waals heterostructure: The graphene Josephson junction (JJ) is made from a van der Waals heterostructure, which consists from bottom to top out of a thick graphite sheet, a bottom hexagonal boron nitride (hBN) with thickness $d = 47.5$ nm, a monolayer graphene and a top hBN (21 nm). We separately prepare the stack by standard polycarbonate-assisted pick-up technique [S1] and place it next to the current anti-node of the resonator. Details about the stacking routine is provided in the SI of Ref. [S2]. In the end of this process the whole device is placed for 1 h in dichlormethane to dissolve polycarbonate residuals to prepare the stacks surface for the following fabrications steps.

Contacting and Shaping: The graphene is contacted and enclosed by a thermally evaporated Ti/Al (5/90 nm) lead, which forms the rf SQUID. Access regions for the self-aligned side contacts [S3] are structured with positive e-beam lithography in combination with CHF₃/O₂ etching. The contacts to the graphene and the loop are fabricated simultaneously, which was done at the Institute of Nanotechnology of the Karlsruhe Institute of Technology (KIT). Rainer Kraft from KIT guided the fabrication, for which we made use of following recipe [S4]:

- Resist: AR-P[©] 672.045 (positive PMMA resist, 950k, 4.5% diluted in anisole)
- Coating: Spin with 300 rpm for 2 s (ramp 1.5 s) followed by 6000 rpm for 60 s (ramp 1.5 s) \rightarrow thickness 280 nm
- EBL: 30 kV acceleration voltage and a dose of 360 $\mu\text{C}/\text{cm}^2$. The 20 μm (120 μm) aperture was used for small (large) structures.
- Resist development: MIBK/IPA 1:3 at room temperature for 20s. The development is followed by 2 s in IPA \rightarrow blow-dry
- Opening hBN windows for edge-contact: Plasma etching in Oxford[©] Plasmalab 80 Plus: CHF₃/O₂ 40 sccm/4 sccm with 60 W at 60 mTorr. The etch time is adjusted to the thickness of the top hBN with calibrated etch rate of 0.55 nm/s.
- Thermal evaporation of Ti/Al contacts in Bestec using the same mask:
 - Ti: $T_{\text{source}} = 1640$ °C; ramp rate 25 °C/min; pressure 7.8×10^{-9} mbar; evaporation rate 0.5 nm/min; film thickness 5 nm, $T_{\text{stage}} = -130$ °C
 - Al: $T_{\text{source}} = 1200$ °C; ramp rate 25 °C/min; pressure 3.5×10^{-9} mbar; evaporation rate 6 nm/min; film thickness 90 nm, $T_{\text{stage}} = 130$ °C
 - The Bestec at KIT has a specially large ratio between source-diameter and source-sample-distance, which is providing substantial undercut deposition.
- Lift-off: 2 h in acetone at room temperature, afterwards rinsed with IPA and blow dried with N₂

After contacting, the graphene stack is shaped to a width $W = 1$ μm using a positive PMMA resist mask in combination with CHF₃/O₂ etching step. This process step is equivalent to the one described above.

Design of the rf SQUID: For the loop material it is desirable to chose a material with low kinetic inductance, because this adds beside the geometric inductance to the total self-inductance of the loop L_{loop} . If $L_{\text{loop}}I_c > \Phi_0/(2\pi)$, where Φ_0 is the flux quantum and I_c is the critical current of a sinusoidal current-phase relation, then the phase φ across the junction becomes hysteretic as a function of external flux due to screening effects, such that the phase condition $\varphi = \pi$ cannot be reached. Therefore we chose Al, which has a low kinetic inductance and a relatively small superconducting gap $\Delta_{\text{Al}} = 180$ μeV advantageous for keeping the critical current low. The elongated shape of the loop and the varying lead width (see Fig. 1 (b) in maintext) builds a compromise between maximizing the coupling to the resonator and minimizing screening effects. For this specific geometry we find a self-inductance $L_{\text{loop}} = 211$ pH from finite-element simulations performed in Sonnet [S5], in which we assume a kinetic sheet inductance of 0.2 pH/ \square for the 90 nm Al film calculated from the value presented in Ref. [S6]. Simultaneously, we obtain the mutual inductance $M = 30.83$ pH between the resonator and the SQUID loop. For both of these results the exact geometry of the device deduced by scanning electron microscope imaging was considered.

The loop surrounds an area $A \approx 4000$ μm^2 implying that already ~ 1 μT generates a flux quantum inside or in other words provides one full phase biasing period. This small magnetic field is governed by the DC current I_{flux} flowing close by the loop.

C. Bonding

After gluing the sample with silver paste onto the copper backplane of the PCB holder, we connect the rf and DC lines from the PCB with Al bond wires to the once of the device. We ensure a homogeneous ground plane by adding many grounding bonds around the resonant structure. Additionally, we place bond-bridges across the TL and between the areas surrounding the rf SQUID. Fig. S1 presents the bond arrangement used for this devices. Note that this pictures is taken after removing the sample from the PCB holder after the measurements and some bonds broke off.

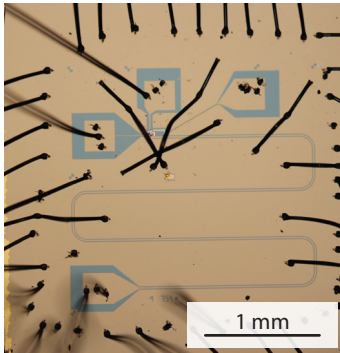


FIG. S1. Optical picture for illustrating the bonding of the device.

SII. SET-UP OVERVIEW

The measurements are carried out in a BlueFors[©] BF-LD400 cryogen-free dilution refrigerator, in which the mixing chamber plate is modified with an additional mounting stage for high frequency components. A detailed overview of the high frequency and DC set-up is provided in Fig. S2. The device is surrounded by a permalloy shield to screen external magnetic field fluctuations. We probe the resonant structure with a vector network analyser (VNA) in a standard reflectometry configuration. The probe signal reaches the sample via an attenuated input line and a directional coupler. The reflected signal travels back to the VNA through the amplification chain consisting of a room temperature amplifier and 4 K-HEMT amplifier, which are isolated towards the device by two circulators located at the mixing chamber plate. The supply lines for the gate and bias voltages of the 4 K-HEMT amplifier are filtered with home-built *LC*-lowpass filters (cut-off ~ 150 kHz). The DC lines for tuning the gate voltage on the graphene and the flux inside the rf SQUID are heavily filtered at room and base temperatures. The Ecosorb[©] lowpass-filter in the high frequency line does have a cut-off frequency around 13 GHz and the silver-epoxy lowpass-filters in the DC lines do have a cut-off around 6 MHz.

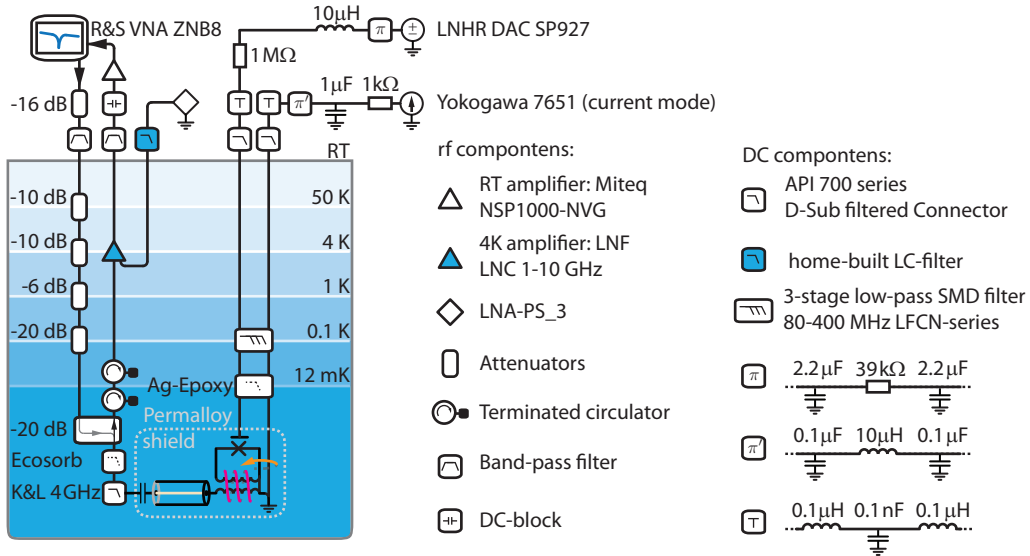


FIG. S2. Detailed overview of the measurement set-up.

III. READ-OUT

The read-out power has a substantial influence on the response of the coupled resonator rf SQUID circuit. In Fig. S3 we present the reflectance coefficient Γ as a function of probe frequency f and probe power VNA_{out} . Here, the graphene JJ is gated with $V_{\text{bg}} = 4.5$ V (electron doped) and tuned to $\varphi = \pi$ (spectral gap is smallest). We observe that for increasing the probe power the resonance frequency shifts to higher values and the resonance lineshape alters. We attribute this to non-linear effects caused by over driving the resonator or saturating the ABS spectrum. It could also be that the stray field of the resonator induces large phase biasing oscillations, which smears out the phase-dependent features of the JJ. Additionally, irradiating JJs affect their current-phase relation [S7] and the IV -characteristics develops Shapiro steps [S8]. Both of the effects will influence the reflective response.

If the read-out power is below -25 dBm, there are no more changes in the resonance frequency nor in the resonance lineshape. All subsequent measurements are carried out with $VNA_{\text{out}} = -30$ dBm and a bandwidth $VNA_{\text{BW}} = 500$ Hz.

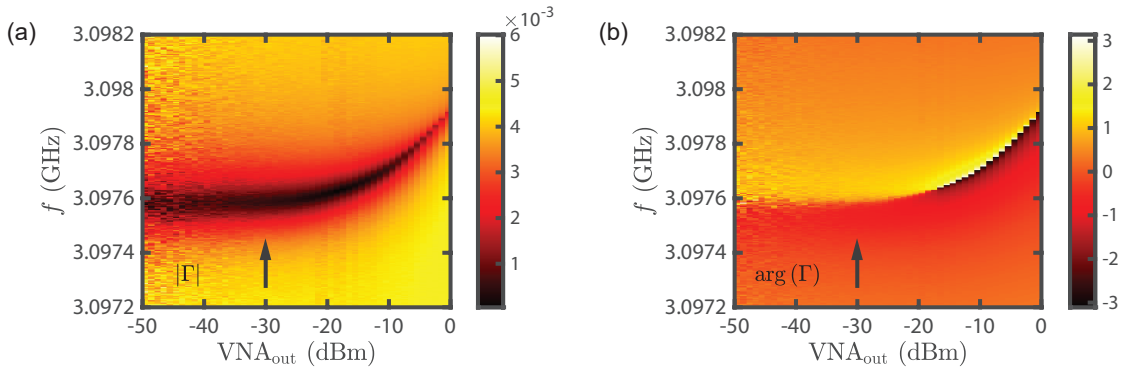


FIG. S3. Reflection coefficient Γ at $V_{\text{bg}} = 4.5$ V and $\varphi = \pi$ as a function of probe frequency f and probe power VNA_{out} obtained with a bandwidth $VNA_{\text{BW}} = 500$ Hz. (a) Amplitude and in (b) argument of Γ . All subsequent measurements are carried out with $VNA_{\text{out}} = -30$ dBm (indicated with the arrows.)

A. Conversion to photon number

The averaged photon number in the resonator can be estimated with following expression [S9]

$$\langle n \rangle = \frac{2}{\hbar\omega_0^2} \frac{Z_0}{Z_r} \frac{Q^2}{Q_c} P_{\text{app}}, \quad (\text{S1})$$

where \hbar is the reduced Planck constant, Z_0 is the environmental impedance, Z_r is the characteristic impedance of the co-planar transmission line, Q is the total quality factor of the resonant structure, Q_c is the coupling quality factor and P_{app} is the applied microwave power. With $\omega_0 = 2\pi \cdot 3.1$ GHz, $Z_0 = 50 \Omega$, $Z_r = 69.5 \Omega$, $Q = 24000$, $Q_c = 24000$ and $P_{\text{app}} = -130$ dBm ($= 10^{-16}$ W) we obtain an intra cavity photon occupation $\langle n \rangle \approx 90$. However this value can deviate from the actual photon number, since P_{app} is only estimated via the total attenuation measured at room temperature in combination with the output power of the VNA.

B. Probe flux $\delta\Phi$

In order to estimate the probe flux $\delta\Phi$ we first evaluate the current at the end of the transmission line (TL) and then translate the current to the magnetic field strength. From TL theory [S10] we can derive a formula, which is expressing the current at the shorted end of a lossless TL capacitively coupled to a generator

$$I_{\text{TL}}(f) = \frac{V_{\text{gen}}}{\sin(\beta l)} \frac{\tan(\beta l)}{jZ_r \tan(\beta l) + Z_0 + (j2\pi f C_c)^{-1}}, \quad (\text{S2})$$

where $V_{\text{gen}} = 10^{\frac{P_{\text{app}}[\text{dBm}] - 10}{10}}$ [V] is the generator voltage, Z_r is the characteristic impedance of the TL, Z_0 is the input impedance of the generator, $\beta = 2\pi f \frac{\sqrt{\epsilon_{\text{eff}}}}{c}$ is the wavenumber of the TL, $\sqrt{\epsilon_{\text{eff}}}$ is the effective refractive index, l is the length of the TL and C_c is the coupling capacitance. By maximizing the absolute value of this expression for the frequency, one obtains the maximal current in the TL provided at resonance. With $P_{\text{app}} = -130$ dBm, $\epsilon_{\text{eff}} = 10.24$, $Z_0 = 50 \Omega$, $Z_r = 69.5 \Omega$, $l = 7.54$ mm and $C_c = 4.7$ fF we obtain $|I_{\text{TL}}|_{\text{max}} = 310$ nA at 3.094 GHz. The Biot-Savart law expresses the magnetic field magnitude B at distance r apart from a long, thin wire, carrying a steady current in free space

$$B = \frac{\mu_0}{2\pi} \frac{I}{r}, \quad (\text{S3})$$

where $\mu_0 = 4\pi \cdot 10^{-7}$ N/A⁻² is the vacuum permeability. By substituting values $I = 310$ nA and $r = 1 \mu\text{m}$ one gets $B = 62$ nT. Furthermore, we are interested in the flux created by this current within a rectangular loop, which can be expressed by

$$\delta\Phi = \frac{\mu_0 I}{2\pi} \cdot d \cdot \ln\left(\frac{s+w}{s}\right), \quad (\text{S4})$$

where d is the length of the loop, w is the width of the loop and s describes the spacing from the wire to the closer loop edge see Fig. S4. With $I = 310$ nA, $d = 80 \mu\text{m}$, $w = 40 \mu\text{m}$ and $s = 1 \mu\text{m}$, which roughly mimics the dimensions of the rf SQUID, we obtain $\delta\Phi \approx 0.01 \Phi_0$, where $\Phi_0 \approx 2 \times 10^{-15}$ Wb is the magnetic flux quantum.

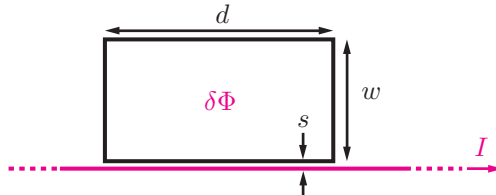


FIG. S4. Rectangular loop next to straight current-carrying wire.

SIV. RESONANCE CURVE FITTING

Changing the flux biasing ($I_{\text{flux}} = [-100, 75] \mu\text{A}$) in the graphene rf SQUID coupled to the $\lambda/4$ -resonator influences the resonant behavior of the circuit as seen in the reflectance curve maps ($V_{\text{bg}} = 5 \text{V}$) presented in Fig. S5(a) and Fig. S5(b). We implement a fitting routine, which is taking into account both the amplitude and the argument of Γ at once to insure a highly robust fitting procedure. An other advantage of the method is the clear distinction between the coupling quality factor Q_c and the effective quality factor Q_e . In the following we consider the resonance curve obtained at $I_{\text{flux}} = -74 \mu\text{A}$. From Fig. S5(c) we observe that $|\Gamma|$ has a shallow asymmetric lineshape and from Fig. S5(d) we observe that $\arg(\Gamma)$ develops a 2π -jump. In the IQ -plane, where $I = \text{Re}(|\Gamma|e^{j\arg(\Gamma)})$ and $Q = \text{Im}(|\Gamma|e^{j\arg(\Gamma)})$, the resonance curve generates here a circle surrounding the IQ -point=(0,0) as shown in Fig. S5(e). We fit both $|\Gamma|$ and $\arg(\Gamma)$ simultaneously with a least-square method with following combination of formulas

$$\Gamma = \left[\frac{\Gamma_{\min} + 2jQ \frac{f-f_0}{f_0}}{1 + 2jQ \frac{f-f_0}{f_0}} - 1 \right] e^{j\phi} + 1, \quad (\text{S5})$$

where $\Gamma_{\min} = \frac{Q_c - Q_e}{Q_c + Q_e}$ is the minimal reflection coefficient in the symmetric case ($\phi = 0$), $Q = (Q_c^{-1} + Q_e^{-1})^{-1}$ is the total quality factor, $Q_e = (Q_i^{-1} + Q_{\text{load}}^{-1})^{-1}$ is the effective quality factor, in which Q_{load} is the quality factor of the load, f is the probe frequency, f_0 is the resonance frequency and ϕ is the asymmetry angle, which causes a rotation of the resonance circle in the IQ -plane around the off-resonance point. In order to account for an offset and a slope in $|\Gamma|$ as well as in $\arg(\Gamma)$, we make use of following expression, which together with Eq. S5 provides the complete fitting formula:

$$\Gamma_{\text{fit}} = |\Gamma| \cdot [a_{\text{off}} + a_{\text{slope}}(f - f_0)] \cdot e^{j[\arg(\Gamma) + p_{\text{off}} + p_{\text{slope}}(f - f_0)]}, \quad (\text{S6})$$

where a_{off} describes an offset in the amplitude, a_{slope} describes a slope in the amplitude, p_{off} describes an offset in the argument and p_{slope} describes a slope in the argument. In Fig. S5 the fit result (solid red) is overlain with the measurement data (blue crosses) and the complete set of fitting parameters is listed.

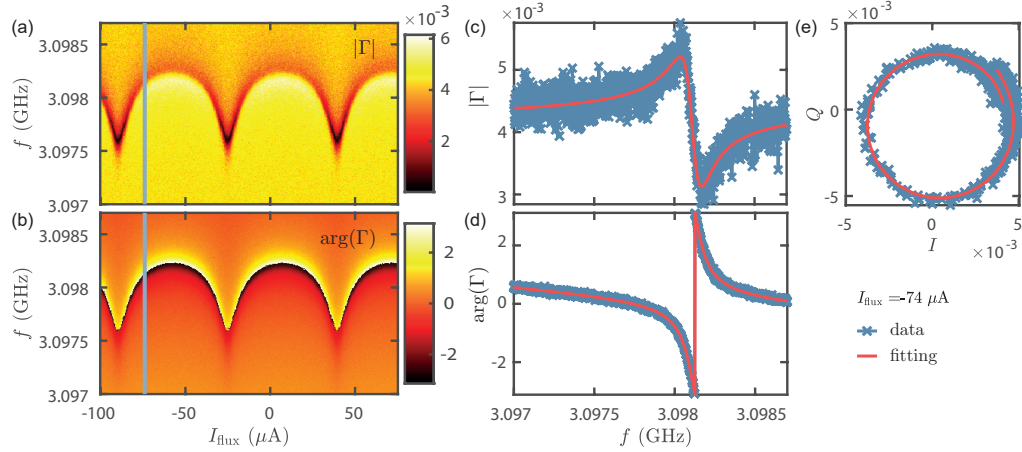


FIG. S5. Flux dependence of the reflection coefficient Γ at $V_{\text{bg}} = 5 \text{V}$. (a)-(b) Colormaps of $|\Gamma|$ and $\arg(\Gamma)$ as a function of probe frequency f and DC flux current I_{flux} . (c)-(d) Resonance curve in $|\Gamma|$ and $\arg(\Gamma)$ at $I_{\text{flux}} = -74 \mu\text{A}$. (e) Resonance curve in the IQ -plane. (c)-(e) The measured data is shown as blue crosses, while the fit result is presented as solid red line. Following parameters are deduced from fitting:

| f_0 | ϕ | Q_c | Q_e | a_{off} | a_{slope} | p_{off} | p_{slope} |
|------------|----------|--------|---------|----------------------|-----------------------------------|------------------|--------------------------------------|
| 3.0981 GHz | 0.25 rad | 23 800 | 669 800 | 4.3×10^{-3} | $5.1 \times 10^{-11} / \text{Hz}$ | 0.16 rad | $-4.7 \times 10^{-7} \text{ rad/Hz}$ |

SV. LOADED RESONATOR

The performance of a resonator is depending on the load impedance Z_{load} attached to it. In order to relate the resonance frequency f_0 and the quality factor Q of the resonator to properties of Z_{load} , one can compare the input impedance of the specific circuit with the one of a known circuit. Here, we will compare a loaded $\lambda/4$ -resonator with a parallel RLC -circuit.

A. Loaded $\lambda/4$ -resonator

In the following we consider a $\lambda/4$ -resonator, in which the normally shorted end is replaced by a load impedance Z_{load} as shown in Fig. S6(a). In general, the input impedance of a transmission line (TL) of length l and characteristic impedance Z_r shunted by Z_{load} is given by

$$Z_{\text{in,TL}} = Z_r \frac{Z_{\text{load}} + Z_r \tanh(\gamma l)}{Z_r + Z_{\text{load}} \tanh(\gamma l)}. \quad (\text{S7})$$

Since the complex propagation constant γ can be expressed as $\gamma = \alpha + j\beta$, where the real part α is the attenuation constant in TL and, the imaginary part β the wavenumber of the TL, we can rewrite

$$\tanh(\gamma l) = \frac{1 - j \tanh(\alpha l) \cot(\beta l)}{\tanh(\alpha l) - j \cot(\beta l)}. \quad (\text{S8})$$

With $\beta = \omega/v_p$, where v_p is the phase velocity of the TL and by introducing the relative frequency $\delta\omega = \omega - \omega_0$ with respect to the resonance frequency ω_0 , the argument of the cot-term becomes

$$\beta l = \frac{\omega_0 l}{v_p} + \frac{\delta\omega l}{v_p}. \quad (\text{S9})$$

The phase velocity at resonance for a quarterwave resonator ($\lambda = 4l$) reads $v_p = \lambda f_0 = 2l \frac{\omega_0}{\pi}$ and therefore

$$\beta l = \frac{\pi}{2} + \frac{\pi \delta\omega}{2\omega_0}. \quad (\text{S10})$$

Assuming $\delta\omega$ being small, we can approximate

$$\cot(\beta l) = \cot\left(\frac{\pi}{2} + \frac{\pi \delta\omega}{2\omega_0}\right) = -\tan\left(\frac{\pi \delta\omega}{2\omega_0}\right) \approx -\frac{\pi \delta\omega}{2\omega_0}. \quad (\text{S11})$$

Assuming that the $\lambda/4$ -resonator is lossless ($\alpha = 0$) we can simplify the input impedance to

$$Z_{\text{in}}^{\lambda/4} = Z_r \frac{Z_{\text{load}} - j Z_r \frac{2\omega_0}{\pi \delta\omega}}{Z_r - j Z_{\text{load}} \frac{2\omega_0}{\pi \delta\omega}}. \quad (\text{S12})$$

In the case of $Z_r \gg \frac{\pi \delta\omega}{2\omega_0} Z_{\text{load}}$, we can write

$$Z_{\text{in}}^{\lambda/4} = \frac{1}{\frac{Z_{\text{load}}}{Z_r^2} + j \frac{\pi \delta\omega}{2\omega_0 Z_r}}. \quad (\text{S13})$$

In general the load impedance is complex valued and can be decomposed into its real and imaginary part, such that $Z_{\text{load}} = \text{Re}(Z_{\text{load}}) + j\text{Im}(Z_{\text{load}})$, which leads to

$$Z_{\text{in}}^{\lambda/4} = \frac{1}{\frac{\text{Re}(Z_{\text{load}})}{Z_r^2} + \frac{j}{Z_r} \left[\frac{\pi \delta\omega}{2\omega_0} + \frac{\text{Im}(Z_{\text{load}})}{Z_r} \right]}. \quad (\text{S14})$$

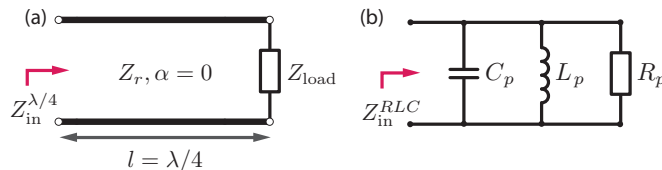


FIG. S6. (a) Loaded quarterwave transmission line. (b) Parallel RLC -circuit.

B. Input impedance of parallel RLC -circuit

We compare this now to a parallel RLC resonant circuit shown in Fig. S6(b). The input impedance of this circuit simply reads

$$Z_{\text{in}}^{RLC} = \left(\frac{1}{R_p} + \frac{1}{j\omega L_p} + j\omega C_p \right)^{-1} \quad (\text{S15})$$

and its resonance frequency is $\omega_0 = 1/\sqrt{L_p C_p}$. Making again use of the relative frequency shift and analysing the circuit near resonance allows us to rewrite the former equation to

$$Z_{\text{in}}^{RLC} \approx \frac{1}{1/R_p + 2j\delta\omega C_p} \quad (\text{S16})$$

or alternatively as

$$Z_{\text{in}}^{RLC} \approx \frac{1}{1/R_p + 2j\sqrt{\frac{C_p}{L_p}} \left(\frac{\delta\omega}{\omega_0} \right)} \quad (\text{S17})$$

Additionally, the internal quality factor of the parallel resonant circuit can be expressed as

$$Q^{RLC} = \omega_0 R_p C_p. \quad (\text{S18})$$

C. Unloaded $\lambda/4$ -resonator

We can describe the special case of an unloaded quarterwave resonance circuit by evaluating Eq. S13 for $Z_{\text{load}} = 0$:

$$Z_{\text{in}}^{\lambda/4} = \frac{1}{j\frac{\pi}{2Z_r} \left(\frac{\delta\omega}{\omega_0} \right)}. \quad (\text{S19})$$

By directly comparing Eq. S19 with Eq. S17 for $R_p \rightarrow \infty$ one finds

$$\frac{\pi}{2Z_r} = 2\sqrt{\frac{C_p}{L_p}}. \quad (\text{S20})$$

One can now determine the capacitance of the equivalent parallel RLC circuit with $\omega_0 = 1/\sqrt{L_p C_p}$ as

$$C_p = \frac{\pi}{4\omega_0 Z_r} \quad (\text{S21})$$

and the inductance of the equivalent circuit as

$$L_p = \frac{4Z_r}{\pi\omega_0}. \quad (\text{S22})$$

In a real experimental scenario the characteristic impedance Z_r is often not known precisely, since besides geometric ingredients – in particular, the capacitance per unit length \mathcal{C}_r and the self-inductance per unit length \mathcal{L}_s – there is also a contribution from material properties, which gives rise to the kinetic inductance per unit length \mathcal{L}_k . Consequently, the characteristic impedance reads $Z_r = \sqrt{\mathcal{L}_r/\mathcal{C}_r}$, where $\mathcal{L}_r = \mathcal{L}_s + \mathcal{L}_k$. Both \mathcal{C}_r and \mathcal{L}_s can be computed with conformal mapping techniques to very high accuracy, whereas \mathcal{L}_k needs to be determined experimentally. \mathcal{L}_k can be measured in a temperature dependence or estimated via the low temperature normal sheet resistance [S11]. In order to circumvent this inconvenience, we can make use of the wavelength λ , which in the case of a lossless transmission line is given by

$$\lambda = \frac{2\pi}{\beta} = \frac{2\pi}{\omega_0 \sqrt{\mathcal{L}_r \mathcal{C}_r}}. \quad (\text{S23})$$

By rearranging this expression at the quarterwave resonance condition and multiplying both sides with \mathcal{C}_r , we find

$$\omega_0 \mathcal{C}_r = \frac{2\pi}{4l\sqrt{\mathcal{L}_r \mathcal{C}_r \frac{1}{\mathcal{C}_r}}}. \quad (\text{S24})$$

Substituting $Z_r = \sqrt{\mathcal{L}_r/\mathcal{C}_r}$ into the previous equation and solve for Z_r leads to

$$Z_r = \frac{2\pi}{4l\omega_0 \mathcal{C}_r}. \quad (\text{S25})$$

This is now a description for Z_r by just geometrical means (l and \mathcal{C}_r) in combination with the resonance frequency ω_0 . Here, we do assume an ideal resonator without any coupling to the environment - however those corrections will be small for large coupling quality factors Q_c . Now inserting Eq. S25 into the expressions for the equivalent circuit (Eq. S21 and S22), we find in agreement with Ref. [S12]

$$C_p = \frac{\mathcal{C}_r l}{2}, \quad (\text{S26})$$

$$L_p = \frac{2}{l\omega_0^2 \mathcal{C}_r}. \quad (\text{S27})$$

D. Evaluating Z_r and L_p

In order to evaluate characteristic properties of the resonant circuit, we make use of conformal mapping techniques derived in Ref. [S13] to express the capacitance per unit length. The effective dielectric constant of a two-layered substrate is found to be

$$\widetilde{\epsilon}_{\text{eff}} = 1 + \frac{\epsilon_{r1} - \epsilon_{r2}}{2} \cdot \frac{K(k_1)K(k'_0)}{K(k'_1)K(k_0)} + \frac{\epsilon_{r2} - 1}{2} \cdot \frac{K(k_2)K(k'_0)}{K(k'_2)K(k_0)} \quad (\text{S28})$$

and the corresponding capacitance per unit length reads

$$\mathcal{C}_r = 4\epsilon_0 \widetilde{\epsilon}_{\text{eff}} \frac{K(k_0)}{K(k'_0)}. \quad (\text{S29})$$

The functions K are the complete elliptical integrals of the first kind, in which

$$\begin{aligned} k_0 &= \frac{s}{s+2w} \\ k_1 &= \frac{\sinh\left(\frac{\pi s}{4h_1}\right)}{\sinh\left(\frac{\pi(s+2w)}{4h_1}\right)} \\ k_2 &= \frac{\sinh\left(\frac{\pi s}{4(h_1+h_2)}\right)}{\sinh\left(\frac{\pi(s+2w)}{4(h_1+h_2)}\right)} \\ k'_i &= \sqrt{1 - k_i^2} \quad \text{with } i = 0, 1, 2, \end{aligned}$$

where s is the central conductor width, w is the spacing to the ground plane, h_1 is the thickness of the top dielectric with relative permittivity ϵ_{r1} and h_2 is the thickness of the bottom dielectric with relative permittivity ϵ_{r2} see Fig. S7.

With $s = 12.1 \mu\text{m}$, $w = 6.1 \mu\text{m}$, SiO_2 thickness $h_1 = 170 \text{ nm}$, Si thickness $h_2 = 500 \mu\text{m}$, SiO_2 permittivity $\epsilon_{r1} = 3.9$, Si permittivity $\epsilon_{r2} = 11.8$ and the vacuum permittivity $\epsilon_0 = 8.854 \times 10^{-12} \text{ F/m}$ we find $\mathcal{C}_r = 153.9 \text{ pF/m}$. With this and the length of the TL $l = 7.54 \text{ mm}$ in combination with the resonance frequency $f_0 \approx 3.098029 \text{ GHz}$ we can now evaluate $Z_r = 69.54 \Omega$ with Eq. S25, $C_p = 580 \text{ fF}$ with Eq. S26 and $L_p = 4.548 \text{ nH}$ with Eq. S27. Note that $\widetilde{\epsilon}_{\text{eff}}$ describes purely the dielectric properties of the TL, whereas ϵ_{eff} also contains properties of the kinetic inductance.

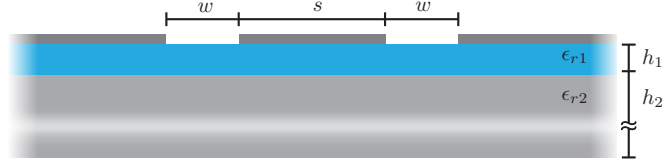


FIG. S7. Cross-section of a transmission line on a layered substrate.

SVI. INFLUENCE OF Z_{load} ON f_0 AND Q_{load}

The resonance condition for a loaded $\lambda/4$ -resonator is fulfilled, when $\text{Im}[Z_{\text{in}}^{\lambda/4}] = 0$, which leads to $\frac{\pi\delta\omega}{2\omega_0} + \frac{\text{Im}[Z_{\text{load}}]}{Z_r} = 0$ deduced from Eq. S14. With the load – the new resonance frequency is called $\omega_0 (= 2\pi f_0)$, while the resonance frequency of the unloaded resonator is called $\omega_{\text{bare}} (= 2\pi f_{\text{bare}})$, hence $\delta\omega = \omega_0 - \omega_{\text{bare}}$. In the limit, $f_0 \approx f_{\text{bare}}$, we can express the resonance frequency shift influenced by the load impedance as

$$\delta f_0 = f_0 - f_{\text{bare}} = -\frac{2}{\pi Z_r} \text{Im}(Z_{\text{load}}) f_{\text{bare}}. \quad (\text{S30})$$

In order to express the quality factor Q_{load} of a loaded quarterwave resonator, we assume that $\frac{\text{Im}[Z_{\text{load}}]}{Z_r} \ll 1$, such that we obtain from Eq. S14

$$Z_{\text{in}}^{\lambda/4} \approx \frac{1}{\frac{\text{Re}(Z_{\text{load}})}{Z_r^2} + \frac{j}{Z_r} \left(\frac{\pi\delta\omega}{2\omega_0} \right)}. \quad (\text{S31})$$

By comparing this expression with Eq. S17, we can conclude that $R_p = \frac{Z_r^2}{\text{Re}(Z_{\text{load}})}$. Combining this finding with Eq. S18 and Eq. S21, we can express the load quality factor as

$$Q_{\text{load}} = \frac{\pi Z_r}{4\text{Re}(Z_{\text{load}})}. \quad (\text{S32})$$

SVII. LOAD IMPEDANCE Z_{load}

Until now we have conducted all derivations for a general load impedance terminating the CTL. In the following we derive an expression to describe the impedance provoked by a loop that is inductively coupled to the shorted end of the CTL. First we consider a transformer configuration with a primary part – the left side in Fig. S8(a) – that consists of an inductor L_1 across which the current I_1 flows and the voltage V_1 develops. The secondary part – the right side in Fig. S8(a) – describes the mutually coupled loop, which is modelled as an inductance L_2 shunted by an impedance Z . The mutual inductance M quantifies the coupling strength between the primary and secondary circuit. In the latter the current I_2 flows and the voltage V_2 appears across L_2 and Z , respectively. The voltages in the two circuits can be described by the transformer equations:

$$V_1 = j\omega L_1 I_1 + j\omega M I_2, \quad (\text{S33a})$$

$$V_2 = -j\omega L_2 I_2 - j\omega M I_1 = Z I_2. \quad (\text{S33b})$$

By rearranging the second equality of Eq. S33b to

$$I_2 = -\frac{j\omega M}{j\omega L_2 + Z} I_1 \quad (\text{S34})$$

one can express the current in the secondary circuit as a function of the current in the primary. The load impedance seen on the side of the primary or resonator, respectively, can be found by inserting Eq. S34 into Eq. S33a and divide both sides by I_1 [S14]:

$$Z_{\text{load}}^* = \frac{V_1}{I_1} = j\omega L_1 + \frac{\omega^2 M^2}{j\omega L_2 + Z}. \quad (\text{S35})$$

Since the frequency shift is determined by the imaginary part of the load impedance (see Eq. S30) and L_1 is constant, the coupling inductance of the primary circuit only provokes an off-set frequency shift. And because the resonance

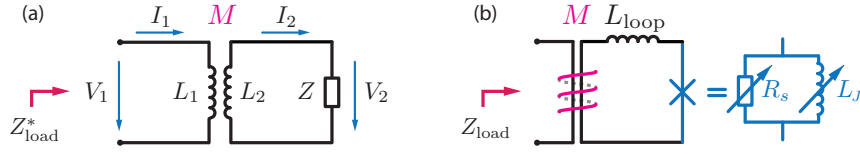


FIG. S8. (a) Transformer with the secondary circuit loaded by impedance Z . (b) Circuit schematic of the inductively coupled rf SQUID, in which the Josephson junction is modelled as variable Josephson inductance L_J in parallel with a variable shunt resistance R_s .

broadening is given by the real part of the load impedance (see Eq. S32), L_1 does not influence the load quality factor. Therefore we neglect L_1 and absorb its contribution in the bare resonance frequency. With this we obtain a simplified expression for the load impedance: $Z_{\text{load}} = \omega^2 M^2 / (j\omega L_2 + Z)$. In the experimental scenario L_2 is the inductance of the SQUID loop L_{loop} and the shunt impedance Z describes the Josephson junction. Here, we model the junction as a tunable Josephson inductance L_J in parallel with a tunable resistor R_s , hence $Z = [1/R_s + 1/(j\omega L_J)]^{-1}$. Consequently, the load impedance in our circuit, as shown in Fig. S8(b), reads

$$Z_{\text{load}} = \frac{\omega^2 M^2}{j\omega L_{\text{loop}} + \left(\frac{1}{R_s} + \frac{1}{j\omega L_J}\right)^{-1}}. \quad (\text{S36})$$

With the load impedance given in Eq. S36 substituted into Eq. S32, we obtain for the load quality factor

$$Q_{\text{load}} = \frac{\pi}{4} \cdot \frac{Z_r}{R_s M^2} \left[L_{\text{loop}}^2 + \frac{(L_J + L_{\text{loop}})^2 R_s^2}{\omega^2 L_J^2} \right]. \quad (\text{S37})$$

Hence, we found a formalism to convert the load quality factor into an effective lumped element model describing the Josephson junction. In the case of $L_J \gg L_{\text{loop}}$ and $\frac{R_s}{\omega L_{\text{loop}}} \gg 1$, we can make the approximation:

$$Q_{\text{load}} \approx \frac{\pi}{4} \cdot \frac{Z_r}{\omega^2 M^2} \cdot R_s. \quad (\text{S38})$$

Assuming $R_s \rightarrow \infty$ in Eq. S36 and making use of Eq. S22, we can approximate Eq. S30 as

$$\delta f_0 \approx \frac{8}{\pi^2} \frac{M^2}{L_p(L_J + L_{\text{loop}})} f_{\text{bare}}, \quad (\text{S39})$$

which describes the frequency shift as a function of the Josephson inductance L_J , which, in turn, is directly related to the current-phase relation (CPR). In general, this last approximation is not needed, but reduces the computational effort tremendously, especially when the iterative screening correction procedure is conducted.

SVIII. COMPARE THE ANALYTICAL EXPRESSIONS WITH NUMERICAL RESULTS

In the following we prove the validity of the analytic formulas for δf_0 and Q_{load} (Eq. S39 and Eq. S37) by comparing their solutions with the numerically evaluated full model. In particular, we generate reflection curve maps and extract from those, the resonance frequency f_0^{full} and the load quality factor $Q_{\text{load}}^{\text{full}}$ by fitting as explained in Sec. SIV. In general, the reflection coefficient reads

$$\Gamma = \frac{Z_{\text{in}}^{\text{full}} - Z_0}{Z_{\text{in}}^{\text{full}} + Z_0}, \quad (\text{S40})$$

where $Z_0 = 50 \Omega$ is the environmental impedance. The coupling capacitance C_c between the measurement set-up and the TL leads to an impedance $Z_c = 1/(j2\pi f C_c)$ in series with the input impedance of the loaded TL, $Z_{\text{in,TL}}$, such that

$$Z_{\text{in}}^{\text{full}} = Z_c + Z_{\text{in,TL}}. \quad (\text{S41})$$

Hence, by combining Eq. S7 and Eq. S36 in Eq. S40 with the use of Eq. S41, we can express Γ as a function of Z_{load} with properties of the TL.

First, we provide a consistency proof for the expression of the frequency shift. In Fig. S9, we keep the shunt resistance $R_s = 100 \text{ M}\Omega$ constant and sweep the Josephson inductance L_J . From the artificial Γ -maps shown in Fig. S9(a)-(b) a clear change in f_0^{full} is observed as a function of L_J , while the lineshape is not affected. Details about the parameters used here are listed in the figure caption. In Fig. S9(c) we overlay the fit results for resonance frequency f_0^{full} of the artificial data (blue circles) with the prediction from the analytic formalism (red, Eq. S39). From Fig. S9(d), which shows the difference Δf_0 between the resonance frequency of the artificial data and the one obtained from the analytic formalism, we observe only slight discrepancies on the order of Hz. Consequently, Eq. S39 describes the resonance frequency as function of L_J to a very high accuracy.

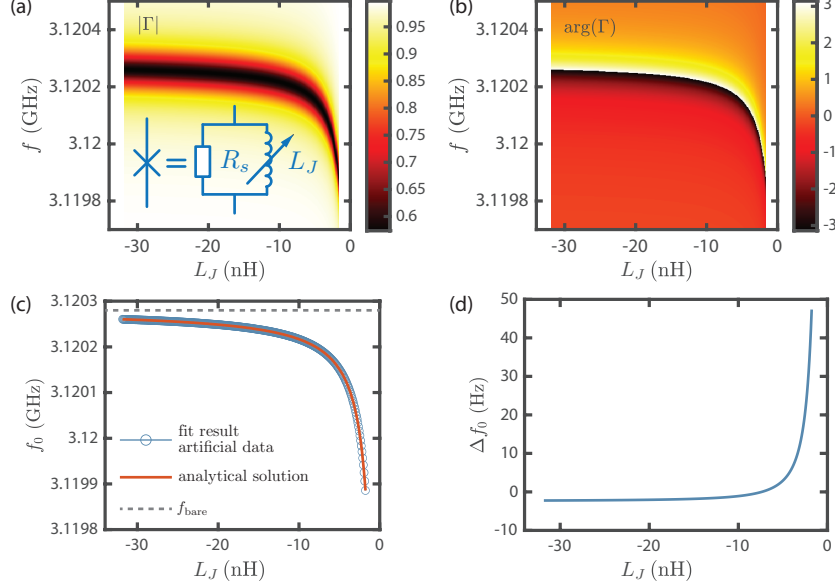


FIG. S9. Parameters for artificial data: $C_c = 4.6 \text{ fF}$, $\alpha = 0.001 \text{ m}^{-1}$, $\beta = 2\pi f \frac{\sqrt{\epsilon_{\text{eff}}}}{c}$, where $\epsilon_{\text{eff}} = 11.225$ and c is the speed of light, $l = 7.1 \text{ mm}$, $Z_r = 64.5 \Omega$, $L_{\text{loop}} = 200 \text{ pH}$, $M = 32 \text{ pH}$, $R_s = 100 \text{ M}\Omega$, sinusoidal CPR $\rightarrow L_J = \frac{2\pi}{\Phi_0 I_c \cos(\varphi)}$, here the sweep range corresponds to the phase biasing condition $\varphi = \pi$ and the critical current is tuned $I_c = 10 \rightarrow 180 \text{ nA}$ (larger I_c produces more shift). (a)-(b) Colormaps of the artificial data $|\Gamma|$ and $\arg(\Gamma)$ as a function of Josephson inductance L_J . (c) The resonance frequency f_0^{full} (blue circles) obtained by fitting the artificial resonance curves. The analytically predicted resonance frequency (red lines) deduced from Eq. S39 with the same parameters as listed above and $f_{\text{bare}} = 3.12028 \text{ GHz}$ obtained from minimizing $|\Gamma|$ for $L_J \rightarrow \infty$ in the full model. (d) Difference between f_0^{full} and the analytically obtained resonance frequency.

Second, we provide a consistency proof for the expression of the load quality factor. In Fig. S10, we keep the Josephson inductance $L_J = -3.2 \text{ nH}$ (sinusoidal CPR with $I_c = 100 \text{ nA}$ at $\varphi = \pi$) constant and sweep the shunt resistance R_s . For simplicity we set $\alpha = 0$, such that the effective quality factor is determined by the load. From the artificial Γ -maps shown in Fig. S10(a)-(b) a clear change the lineshape of the resonance curve as a function of R_s is observed. Details about the parameters used here are listed in the figure caption. The dark region in Fig. S10(a), where $|\Gamma| = 0$ corresponds to full matching, where $Q_c = Q_{\text{load}}$. For small R_s values the resonator becomes overcoupled ($Q_c > Q_{\text{load}}$) and $\arg(\Gamma)$ evolves smoothly, whereas for large R_s values the resonator becomes undercoupled ($Q_c < Q_{\text{load}}$) and $\arg(\Gamma)$ undergoes a 2π -leap. The coupling quality factor can be expressed as $Q_c = \frac{\pi}{4\omega^2 Z_0 Z_r C_c^2}$, for which we find $Q_c = 29950$ with the model parameters $C_c = 4.6 \text{ fF}$, $Z_r = 64.5 \Omega$ and $\omega \approx 2\pi \cdot 3.12 \text{ GHz}$. In Fig. S10(c) we overlay the fit results for Q_{load} of the artificial data (blue circles) and the prediction from the analytic formalism (red, Eq. S37). From Fig. S10(d), which presents the difference ΔQ_{load} between the artificial data and the predications, we observe very small discrepancies. Since, R_s is naturally present in $\text{Im}(Z_{\text{load}})$, changing the resistance causes in addition a small shift of the resonance frequency. By the comparison between the resonance frequency of the artificial data and the one obtained analytically (assumption $R_s \rightarrow \infty$, such that Eq. S39 becomes valid) shown in Fig. S10(e), we observe a discrepancy of $\sim 6 \text{ kHz}$ for the smallest R_s value. On a first glance this seems a lot, one should however relate this number with the overall shift of the resonance frequency coming from $L_J = -3.2 \text{ nH}$, which is about 200 kHz . Hence, the error induced by neglecting R_s , is on the order of a few % as long as $R_s \geq 100 \Omega$, which is the case for our measurement.

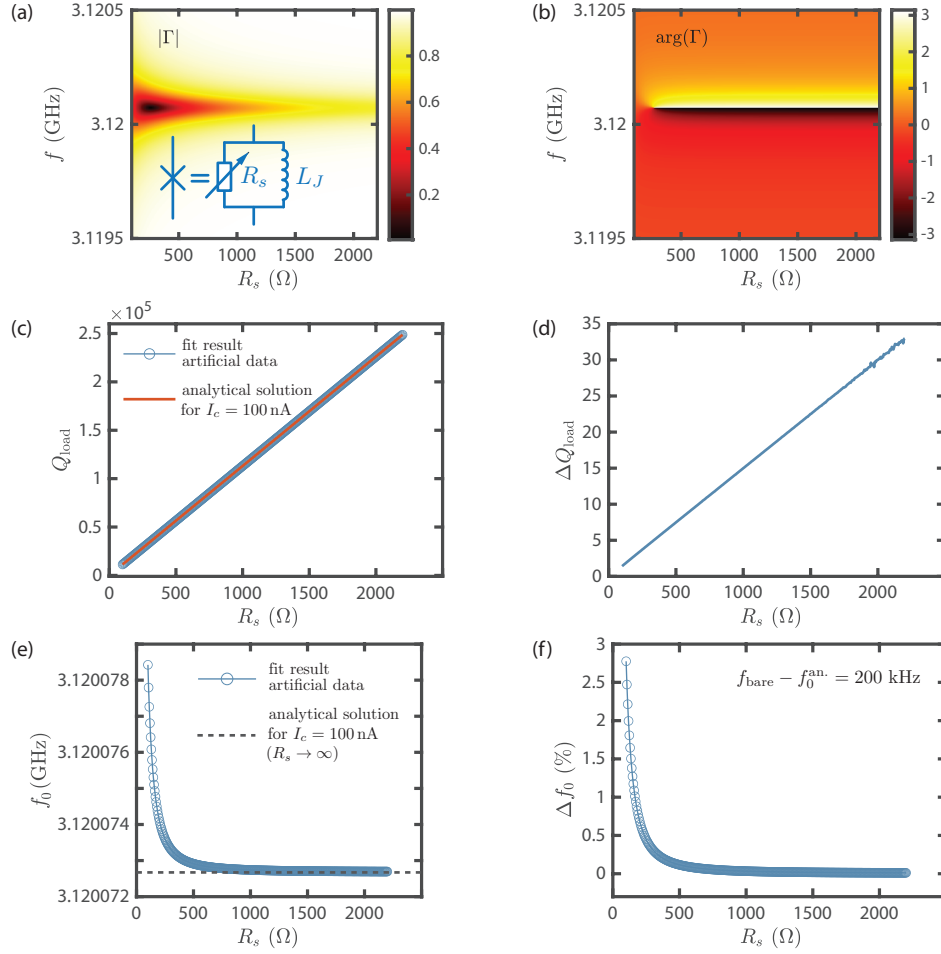


FIG. S10. Parameters for artificial data: $C_c = 4.6$ fF, $\alpha = 0$, $\beta = 2\pi f \frac{\sqrt{\epsilon_{\text{eff}}}}{c}$, where $\epsilon_{\text{eff}} = 11.225$ and c is the speed of light, $l = 7.1$ mm, $Z_r = 64.5$ Ω , $L_{\text{loop}} = 200$ pH, $M = 32$ pH, $I_c = 100$ nA, $L_J = -\Phi_0/(2\pi I_c) = -3.183$ nH. (a)-(b) Colormaps of the artificial data $|\Gamma|$ and $\arg(\Gamma)$ as a function of shunt resistance R_s . (c) The load quality factor Q_{load} (blue circles) obtained by fitting the artificial resonance curves as a function of R_s . The analytically predicted load quality factor (red lines) deduced from Eq.S37 with the same parameters as listed above and $f_{\text{bare}} = 3.12028$ GHz obtained from minimizing $|\Gamma|$ for $L_J \rightarrow \infty$ and $R_s \rightarrow \infty$ in the full model. (d) Difference between $Q_{\text{load}}^{\text{full}}$ and the analytically obtained load quality factor. (e) The resonance frequency f_0^{full} (blue circles) obtained by fitting the artificial resonance curves and predicted resonance frequency for $L_J = -3.2$ nH. (f) Relative error between the actual resonance frequency shift and the predicted resonance frequency shift $f_0^{\text{an.}}$; $\Delta f_0(\%) = (f_0^{\text{full}} - f_0^{\text{an.}})/(f_{\text{bare}} - f_0^{\text{an.}})$.

SIX. CURVE FITTING WITH SCREENING CORRECTION

Using Eqs. 5, 6 and 7 from the maintext, we express the shifted resonance frequency f_0 as a function of the junction phase φ ,

$$f_0(\varphi) = \left[\frac{8}{\pi^2} \frac{M^2}{L_p \left(\left(\frac{2\pi}{\Phi_0} \sum_{k=1}^{k_{\max}} (-1)^{k-1} A_k k \cos(k\varphi) \right)^{-1} + L_{\text{loop}} \right)} + 1 \right] f_{\text{bare}}. \quad (\text{S42})$$

We fix the values of $M = 30.83$ pH, $L_{\text{loop}} = 211$ pH and $L_p = 4.546$ nH obtained from simulations, and treat A_k and f_{bare} as free fitting parameters.

In the absence of current in the rf SQUID loop, the junction phase φ is solely determined by the external magnetic flux Φ in the loop, $\varphi = \varphi_{\text{ext}} = 2\pi\Phi/\Phi_0$. Taking into account the flux created by the circulating DC supercurrent yields

$$\varphi = \varphi_{\text{ext}} - \frac{2\pi}{\Phi_0} L_{\text{loop}} I_s(\varphi). \quad (\text{S43})$$

This means, that the junction phase φ depends on the external flux and the CPR to-be-determined as well.

In the experiment the resonance frequency f_0 is measured as a function of the current in the flux line. Using the periodicity of the signal, we convert the flux current to the external phase φ_{ext} by applying a linear transformation. Next, to determine the CPR from the $(f_0, \varphi_{\text{ext}})$ data while taking into account the flux contribution of the supercurrent, we find the self-consistent solution of Eqs. S42 and S43 with an iterative method. The scheme is presented with the pseudocode in Algorithm 1. Essentially, it combines fixed-point iteration with Eq. S43 and least-square fits to Eq. S42. The procedure realizes the non-linear transformation of φ_{ext} to φ , and outputs the harmonic coefficients A_k and the bare resonance frequency f_{bare} .

Algorithm 1 Iterative procedure for curve fitting with screening correction

```

function FITWITHSCREENING( $f_0, \varphi_{\text{ext}}; M, L_p, L_{\text{loop}}, n_{\text{iter}} = 30, \alpha = 0.2 \dots 0.4, k_{\max} = 10$ )
   $\varphi = \varphi_{\text{ext}}$  ▷ Initialization
  for  $n_{\text{iter}}$  repetitions do
     $A_k, f_{\text{bare}} \leftarrow$  least-square fit of  $(f_0, \varphi)$  data points to Eq.(S42)
     $I_s(\varphi) = \sum_{k=1}^{k_{\max}} (-1)^{k-1} A_k \sin(k\varphi)$  ▷ Substitution of  $A_k$  into Eq. 7
     $\varphi^{\text{new}} = \varphi_{\text{ext}} - 2\pi/\Phi_0 \cdot L_{\text{loop}} I_s(\varphi)$  ▷ Substitution of  $I_s$  into Eq. S43
     $\varphi = \alpha \varphi^{\text{new}} + (1 - \alpha) \varphi$  ▷ Smooth update
  end for
  return  $A_k, f_{\text{bare}}, \varphi$ 
end function

```

In the following we illustrate the fitting routine with the experimental data obtained at $V_{\text{bg}} = 6$ V. In Fig. S11 the initialization is shown, whereas the iteration and the outcome of the algorithm is illustrated in Figs. S12-S13. The convergence of the procedure has been checked manually for each gate voltage. Depending on the values of M and L_{loop} , manual tuning of the smoothing parameter α was necessary.

Figs. S12(c) and S13(c) show that neglecting the flux contribution of the supercurrent, and using the approximation $\varphi = \varphi_{\text{ext}}$ leads to overestimating the skewness of the CPR. While the apparent skewness parameter in this approximation is $S_{\text{ext}} = 0.2434$, the self-consistent solution yields $S = 0.2168$. Similarly, the harmonic coefficient ratio reduces from $A_2/A_1 \approx 0.185$ to $A_2/A_1 \approx 0.165$ as the iteration converges.

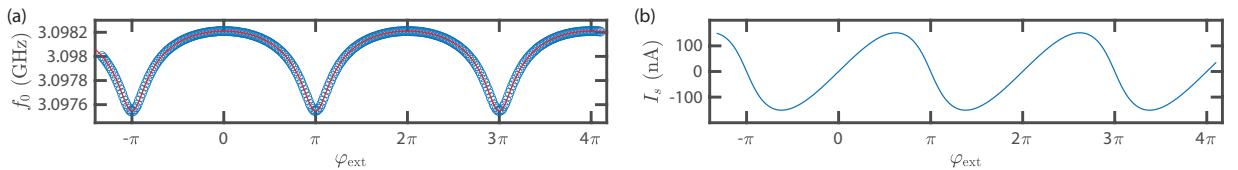


FIG. S11. (a) Extracted resonance frequency f_0 (blue circles) as a function of external phase φ_{ext} at $V_{\text{bg}} = 6$ V. From the fit (solid red, Eq. S42) one obtains the supercurrent $I_s(\varphi_{\text{ext}})$ as a function of external phase shown in (b).

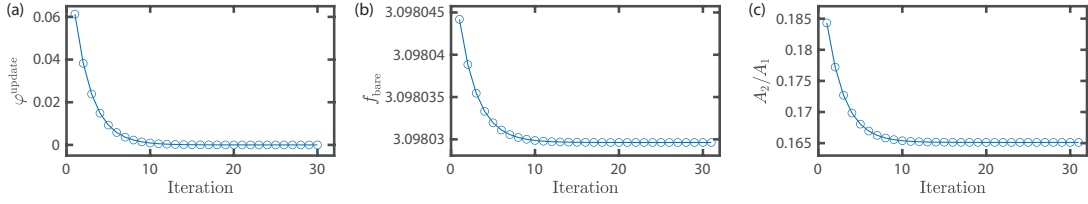


FIG. S12. Convergence of the iterative curve fitting method ($V_g = 6$ V, $\alpha = 0.4$). (a) The magnitude of the phase update, $\varphi^{\text{update}} = \langle |\varphi^{\text{new}} - \varphi| \rangle_{\text{avg}}$ converges to zero as the iteration progresses. (b-c) Convergence of the bare resonance frequency f_{bare} and the harmonic coefficient ratio A_2/A_1 .

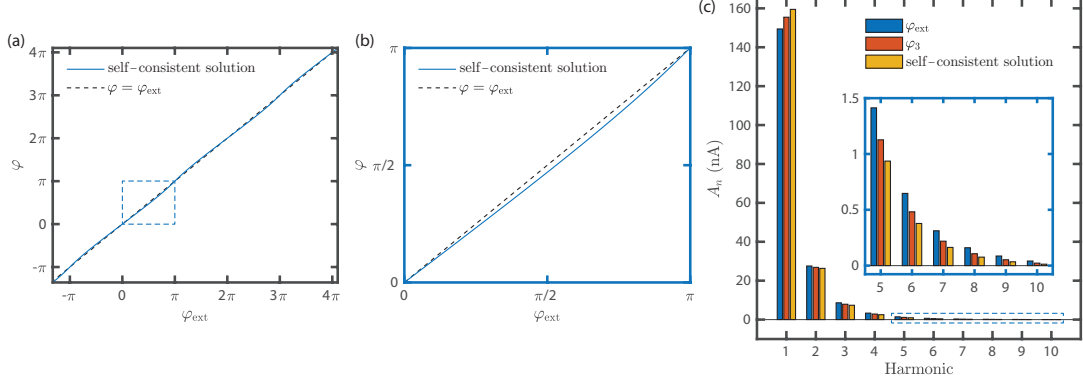


FIG. S13. Outcome of the iterative curve fitting method ($V_{\text{bg}} = 6$ V) (a-b) Junction phase φ as a function of the external phase $\varphi_{\text{ext}} = 2\pi\Phi/\Phi_0$. The self-consistent solution of the equation set (continuous, blue) deviates from the $\varphi = \varphi_{\text{ext}}$ line (dashed black). (c) Harmonic coefficients A_k at different stages of the iteration: initial solution (corresponding to the $\varphi = \varphi_{\text{ext}}$ approximation), solution at $n_{\text{iter}} = 3$ and $n_{\text{iter}} = 30$ (converged).

SX. CHARGE CARRIER DENSITY:

To convert the applied back gate voltage (V_{bg}) to charge carrier density (n_g) we used a plate capacitor model including the quantum capacitance of graphene [S15], which results in

$$e(V_{\text{bg}} + V_{\text{off}}) = \frac{e^2 n_g d}{\epsilon_0 \epsilon_r} + \text{sgn}(n_g) \hbar v_F \sqrt{\pi |n_g|}, \quad (\text{S44})$$

where $V_{\text{off}} = 0.44$ V is the offset voltage of the charge neutrality point with respect to 0 V, e is the electron charge, $d = 47.5$ nm the thickness of the gate dielectric, $\epsilon_0 = 8.854 \times 10^{-12}$ F/m the vacuum permittivity, $\epsilon_r = 3.8$ the dielectric constant of hBN [S16], \hbar the reduced Planck constant, and $v_F = 10^6$ m/s the Fermi velocity of graphene. The quantum capacitance corresponding to the second term on the right hand side of Eq. S44 leads to minor deviations of the linear behavior on n_g with respect to V_{bg} around charge neutrality, as shown in Fig. S14 (a). By using Eq. S44 the previously extracted critical current $I_c(V_{\text{bg}})$ is plotted as a function of n_g in Fig. S14 (b). In previous works oscillations of $I_c(n_g)$ were observed for negative densities for high mobility and ballistic graphene Josephson junctions [S17, S18]. They arise due to quantum interference of the electrons moving in a Fabry-Pérot cavity [S19], which is formed by potential steps in the graphene. Namely, the graphene is n' -doped with electrons close to the contacts given by the work function mismatch of the graphene and the Al boundary, while the bulk of graphene is p -doped with holes due to the negative applied V_{bg} . The oscillations show their m^{th} maxima at $\sqrt{n_g} = m\sqrt{\pi}/L$, where L corresponds to the length of the cavity. Nevertheless, no such oscillations were observed in our measurement of $I_c(n_g)$, which indicates that the electron transport is diffusive in our sample.

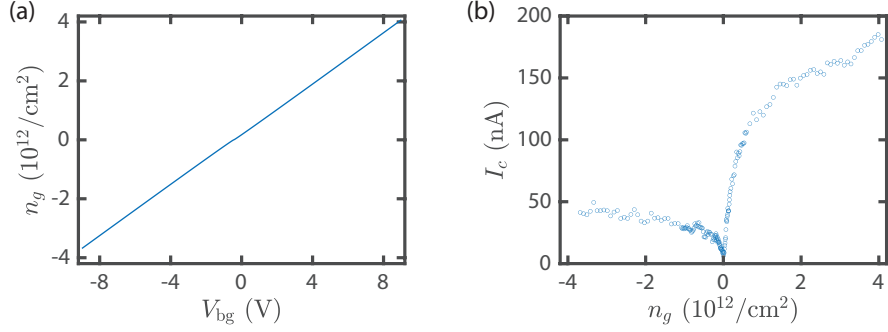


FIG. S14. (a) Charge carrier density n_g determined with Eq.S44 as function of gate voltage V_{bg} . (b) Critical current I_c as function of n_g .

SXI. TEMPERATURE DEPENDENCE:

A. Theoretical description

We numerically solve the time-dependent Usadel equation [S20, S21], from which we infer the inductive B_J and dissipative G_s microwave response of a short diffusive Josephson junction. The theoretical predictions are based on characteristic energy scales: The electronic temperature T , the photonic energy hf irradiating on the junction, the relaxation rate γ , the superconducting gap Δ and the Thouless energy E_T .

In Fig. S15, we fix $\Delta/E_T = 0.1$ and $hf/E_T = 0.01$. On the left axis the dissipative response normalized with the normal state conductance G_s/G_N is plotted (solid blue lines) and on the right axis the inductive response normalized with the normal state conductance B_J/G_N is plotted (dashed red lines).

In Fig. S15(a) we fix $\gamma/E_T = 0.02$, while we sweep the temperature ratio kT/E_T . The wide onset of the dissipation peak even at low temperatures is mainly due to the non-vanishing relaxation ratio γ/E_T causing lifetime broadening of the ABS spectrum. With increasing temperature the conductance peak shrinks and becomes wider. A plateau like feature turning into a double wall can be recognized at $\varphi = \pi$ due to the dynamics of the thermally populated E_n^+ -states. From the susceptance we observe that the conditions for $B_J/G_N = 0$ are moving away from $\varphi = \pi$ for increasing temperature and the absolute values of B_J/G_N at $\varphi = \pi$ and $\varphi = 0, 2\pi$ approach each other, which means that the CPR is becoming more sinusoidal.

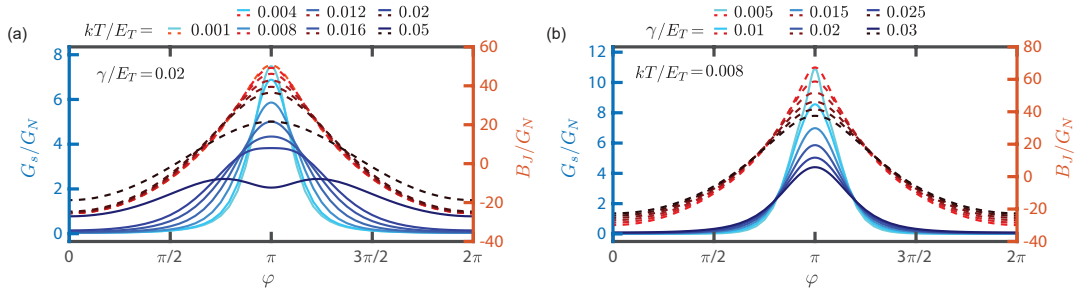


FIG. S15. Numerical simulations of the shunt conductance G_s/G_N and junction susceptance B_J/G_N both normalized with the normal state conductance G_N . Fixed parameters $\Delta/E_T = 0.1$ and $hf/E_T = 0.01$. (a) Dissipative (left) and inductive (right) microwave response for different temperatures but fixed relaxation rate. (b) Dissipative (left) and inductive (right) microwave response for different relaxation rates but fixed temperature.

For comparison we present in Fig. S15(b) the numerical results for fixing $kT/E_T = 0.008$, while sweeping the relaxation ratio γ/E_T . We recognize a less evident change of the dissipation peak center as compared to the temperature sweep. Overall the conductance peak broadens accompanied with a shrinking of the height. Importantly, here the susceptance reveals as well a reduction of the CPR skewness. Note, that this plot is the same as Fig. 7(d) in the maintext, but globally normalized with G_N . Since the temperature effect seem to evolve differently from the relaxation rate dependence – both of this parameters should be accessible by comparing theoretical predications with experimental data.

B. Experimental results

From theory it is predicted that for increasing the temperature T the current-phase relation (CPR) becomes more and more sinusoidal, which is due to the balancing between E_n^+ - and E_n^- -states described by the Fermi-Dirac distribution. The population of E_n^+ -states further affects the absorbcency of the ABS spectrum, because transition from $E_n^- \rightarrow E_n^+$ are prohibited if the final state is already occupied. As a consequence the dissipation peak becomes smaller.

In the following we probe the microwave response of the graphene JJ in terms of the CPR and the phase-dependent dissipation at $V_{\text{bg}} = 12\text{ V}$ for different temperatures. We deduce the CPR and the shunt conductance with the same methods described above and in the maintext. In Fig. S16(a) we illustrate the self-consistent CPR solution for different base temperatures adjusted by heating the mixing chamber plate. We observe a clearly skewed CPR for temperatures far below the critical temperature of Al ($T_c \approx 1.2\text{ K}$), while for $T \rightarrow T_c$ the skewness as well as the critical current I_c decreases as present separately in Figs. S16(b)-(c). These effects are attributed to: i) the washing out of the energetically low lying states (close to $E = 0$), which are responsible for the skewness due to their high transparency and ii) the closing of the superconducting gap. Measurements for $T > 900\text{ mK}$ were suffering from strong temperature fluctuations.

As postulated by theory we obtain a counter-intuitive decreasing of the dissipation peaks for increasing temperatures as seen in Fig. S16(d). Not only the height is influenced by the temperature, but also the width, which is also a result from the theoretical predictions. We fit the different dissipation peaks with a Lorentzian function of the form $L = \frac{a(b/2)^2}{(\varphi-c)^2+(b/2)^2} + d$, where a is a scaler for the peak height, b is the full-width-half-maximum (FWHM), c is a translation on the phase-axis and d describes a vertical offset. We find that the averaged FWHM of the two peaks measured at the same temperature is increasing $\langle \text{FWHM} \rangle \approx 0.2\pi \rightarrow \pi$ for temperatures $T = 20 \rightarrow 600\text{ mK}$, while the peak height shrinks by a factor of ~ 3 .

In contrast to the low temperature results presented in the maintext (Fig. 8) we did not find combinations of kT/E_T and γ/E_T , which simultaneously reproduce the inductive and dissipative response. We attribute this to the granularity of parameter space used in the simulation. In order to describe the microwave behavior of the JJ at high temperatures – effects like highly enhanced relaxation rates, modifications in junction length limit and the gap closing would need to be considered.

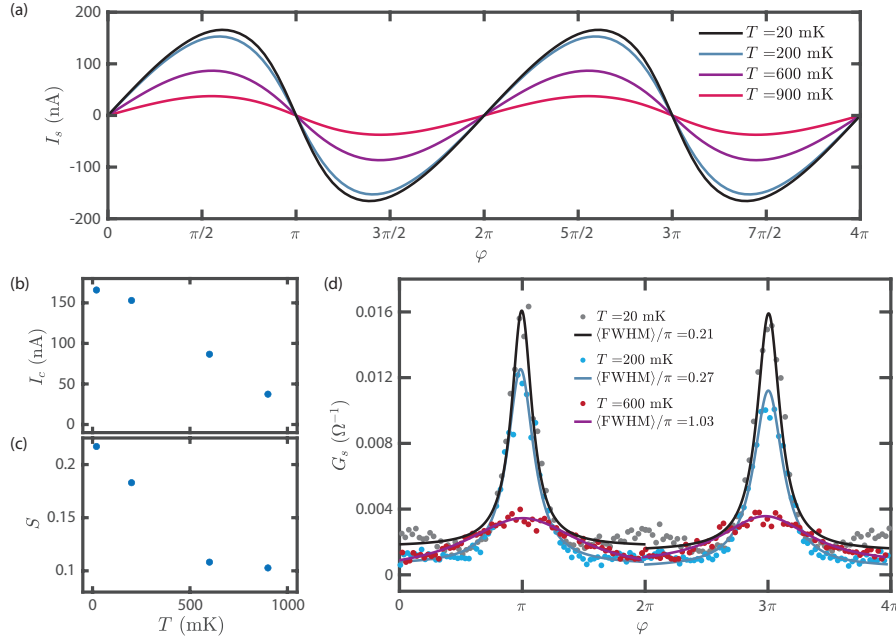


FIG. S16. Temperature T dependence at $V_{\text{bg}} = 12\text{ V}$. (a) Self-consistent CPR for different temperatures (see legend). (b) Critical current I_c as a function of T . (c) Skewness parameter S as a function of T . (d) Phase-dependent dissipation at different T . The peaks are fitted with Lorentzian functions, which reveals a clear spreading of the width for increasing T .

-
- [S1] P. J. Zomer, M. H. D. Guimarães, J. C. Brant, N. Tombros, and B. J. van Wees, Fast pick up technique for high quality heterostructures of bilayer graphene and hexagonal boron nitride, *Appl. Phys. Lett.* **105**, 013101 (2014).
- [S2] D. I. Indolese, P. Karnatak, A. Kononov, R. Delagrèze, R. Haller, L. Wang, P. Makk, K. Watanabe, T. Taniguchi, and C. Schönenberger, Compact SQUID Realized in a Double-Layer Graphene Heterostructure, *Nano Lett.* **20**, 7129 (2020).
- [S3] L. Wang, I. Meric, P. Y. Huang, Q. Gao, Y. Gao, H. Tran, T. Taniguchi, K. Watanabe, L. M. Campos, D. A. Muller, J. Guo, P. Kim, J. Hone, K. L. Shepard, and C. R. Dean, One-Dimensional Electrical Contact to a Two-Dimensional Material, *Science* **342**, 614 (2013).
- [S4] R. Kraft, J. Mohrmann, R. Du, P. B. Selvasundaram, M. Irfan, U. N. Kanilmaz, F. Wu, D. Beckmann, H. von Löhneysen, R. Krupke, A. Akhmerov, I. Gornyi, and R. Danneau, Tailoring supercurrent confinement in graphene bilayer weak links, *Nat. Commun.* **9**, 1722 (2018).
- [S5] E. U. Manual, Sonnet software, Inc., Liverpool, NY , 50 (2005).
- [S6] J. Hu, M. Salatino, A. Traini, C. Chaumont, F. Boussaha, C. Goupil, and M. Piat, Proximity-Coupled Al/Au Bilayer Kinetic Inductance Detectors, *J. Low Temp. Phys.* **199**, 355 (2020).
- [S7] J. Basset, M. Kuzmanović, P. Virtanen, T. T. Heikkilä, J. Estève, J. Gabelli, C. Strunk, and M. Aprili, Nonadiabatic dynamics in strongly driven diffusive Josephson junctions, *Phys. Rev. Res.* **1**, 032009 (2019).
- [S8] S. Shapiro, Josephson currents in Superconducting tunneling: The effect of microwaves and other observations, *Phys. Rev. Lett.* **11**, 80 (1963).
- [S9] J. Burnett, A. Bengtsson, D. Niepce, and J. Bylander, Noise and loss of superconducting aluminium resonators at single photon energies, *J. Phys. Conf. Ser.* **969**, 012131 (2018).
- [S10] D. M. Pozar, *Microwave engineering* (John Wiley & sons, 2011).
- [S11] J. Zmuidzinas, Superconducting Microresonators: Physics and Applications, *Annu. Rev. Condens. Matter Phys.* **3**, 169 (2012).
- [S12] M. Göppl, A. Fragner, M. Baur, R. Bianchetti, S. Filipp, J. M. Fink, P. J. Leek, G. Puebla, L. Steffen, and A. Wallraff, Coplanar waveguide resonators for circuit quantum electrodynamics, *J. Appl. Phys.* **104**, (2008).
- [S13] S. Gevorgian, Basic characteristics of two layered substrate coplanar waveguides, *Electron. Lett.* **30**, 1236 (1994).
- [S14] F. E. Terman, *Electronic and radio engineering* (McGraw-Hill, 1955).
- [S15] J. Xia, F. Chen, J. Li, and N. Tao, Measurement of the quantum capacitance of graphene, *Nat. Nanotechnol.* **4**, 505 (2009).
- [S16] A. Laturia, M. L. Van de Put, and W. G. Vandenberghe, Dielectric properties of hexagonal boron nitride and transition metal dichalcogenides: from monolayer to bulk, *npj 2D Mater. Appl.* **2**, 6 (2018).
- [S17] M. T. Allen, O. Shtanko, I. C. Fulga, J. I. Wang, D. Nurgaliev, K. Watanabe, T. Taniguchi, A. R. Akhmerov, P. Jarillo-Herrero, L. S. Levitov, and A. Yacoby, Observation of Electron Coherence and Fabry-Perot Standing Waves at a Graphene Edge, *Nano Lett.* **17**, 7380 (2017).
- [S18] V. E. Calado, S. Goswami, G. Nanda, M. Diez, A. R. Akhmerov, K. Watanabe, T. Taniguchi, T. M. Klapwijk, and L. M. K. Vandersypen, Ballistic Josephson junctions in edge-contacted graphene, *Nat. Nanotechnol.* **10**, 761 (2015).
- [S19] A. F. Young and P. Kim, Quantum interference and Klein tunnelling in graphene heterojunctions, *Nat. Phys.* **5**, 222 (2009).
- [S20] K. D. Usadel, Generalized diffusion equation for superconducting alloys, *Phys. Rev. Lett.* **25**, 507 (1970).
- [S21] P. Virtanen, F. S. Bergeret, J. C. Cuevas, and T. T. Heikkilä, Linear ac response of diffusive SNS junctions, *Phys. Rev. B* **83**, 144514 (2011).